Theoretical Minimum Uncertainty of Single-Molecule Localizations Using a Single-Photon Avalanche Diode Array

Quint Houwink

TUDelft
Delft University of Technology

Delft Center for Systems and Control

Theoretical Minimum Uncertainty of Single-Molecule Localizations Using a Single-Photon Avalanche Diode Array

MASTER OF SCIENCE THESIS

For the degree of Master of Science in Systems and Control at Delft University of Technology

Quint Houwink

July 16, 2021

Faculty of Mechanical, Maritime and Materials Engineering (3mE) · Delft University of Technology

DELFT UNIVERSITY OF TECHNOLOGY
DEPARTMENT OF
DELFT CENTER FOR SYSTEMS AND CONTROL (DCSC)

The undersigned hereby certify that they have read and recommend to the Faculty of Mechanical, Maritime and Materials Engineering (3mE) for acceptance a thesis entitled

THEORETICAL MINIMUM UNCERTAINTY OF SINGLE-MOLECULE LOCALIZATIONS USING A SINGLE-PHOTON AVALANCHE DIODE ARRAY

by

QUINT HOUWINK

in partial fulfillment of the requirements for the degree of

MASTER OF SCIENCE SYSTEMS AND CONTROL

Dated: <u>July 16, 2021</u>

Supervisor(s):

<div align="right">

_____

dr.ir. C.S. Smith

</div>

Reader(s):

<div align="right">

_____

dr.ir. S. Wahls

</div>

<div align="right">

_____

dr.ir. R.A. Norte

</div>

Abstract

Optical microscopes are fundamentally limited to a resolution of several hundreds of nanometers by the diffraction of light. Single-molecule localization microscopy (SMLM) circumvents this limit by sparsely exciting fluorescent molecules at different time instances. Single molecules can subsequently be localized with improved precision over the diffraction limit. Due to their high frame rate, single-photon avalanche diode (SPAD) arrays are imagers that can be used for SMLM. Most SPADs have to recharge after each photon arrival. During this recharging period, the SPAD is insensitive to more photon arrivals. As a result, SPAD arrays will measure zero or one photons for each pixel in each frame, whereas scientific complementary metal-oxide semiconductor (sCMOS) imagers and electron multiplying charge-coupled devices (EMCCD) have a discrete frame output. Here, we describe the photon arrivals in the image formation model of the SPAD array as a binomial process rather than as a Poissonian process. In addition, we quantify the minimum theoretical uncertainty of single-molecule localizations using a binomial Cramér-Rao lower bound and benchmark it with simulated and experimental data. We show that if the expected photon count is larger than one for all pixels within one standard deviation of a Gaussian point spread function, the binomial CRLB gives a 46% higher theoretical uncertainty than the Poissonian CRLB. Without saturation, which is the case for most SMLM applications, the binomial CRLB model gives the same uncertainty as the Poissonian CRLB. Therefore, the binomial CRLB can be used to predict and benchmark localization uncertainty for SMLM with SPAD arrays for all practical emitter intensities.

Keywords: *Single-Molecule Localization Microscopy, Single-Photon Avalanche Diode Array, Cramér-Rao Lower Bound*

Table of Contents

List of Figures

Preface

The first time I heard about the wondrous world of super-resolution microscopy, my mind started painting a picture. I would imagine floating around in the sample with around me molecules like planets in a solar system. As I learned about the deeper working of this world, the painting gathered color and dangers arose. Photons would soar past me and collide with the planets, igniting them into giant balls of neon light. Some planets might drift out of sight, entering darker, more permanent, phases of their lives. I would jump onto one of the photons and ride it through the objective and into the world of lenses and mirrors. On ambitious days, I would attempt to invade the imaging device and battle dark currents eager to release spontaneous avalanches. Then I would try to stop those avalanches, but I would get stuck in the matrices of the digital world. All of those journeys combined helped to make the painting detailed, unique and above all, true. The painting is now finished, I decided to call it 'my thesis' and I added a bit of myself to it.

To all those visiting my thesis; I hope that my contribution helps you on your journeys.

While I might have been the one holding the brush, there would have been no result without the help of many pairs of eyes and brains. Let me start with thanking my thesis supervisor, Carlas, who was there from start to finish and always willing to assist with his impressive experience in the field. For all the questions that arose daily on the topic of super-resolution microscopy, mathematics or thesis writing I would find my way to Dylan. I have always appreciated our lengthy discussions on Monday, which helped kick-start my week and challenged me to critical thinking. All of the hours in the lab, staring at white noise, hoping for a molecule to appear, would not have been possible, or bearable, without the help of Jelmer, Shih-Te and Daniel. Thank you all for your assistance and perseverance with the SPAD array setup. Also, I would like to extend my gratitude to the other MSc. students in Carlas' group. Their insights and feedback during Tuesday meetings and practice presentations have helped shape this thesis.

Finally, there are those who allowed me to explain the fascinating world of super-resolution microscopy to them, and were even genuinely interested. I am talking about my amazing parents, my loving girlfriend and my thoughtful friends. Without your support and affection, this pandemic-struck year would not have been such a joyful period of my life. I am truly grateful for having all of you around.

<div align="right">

Quint Houwink
July 16, 2021

</div>

‘ “I may not be as strong as I think,’ the old man said.
‘But I know many tricks and I have resolution.’ ”

— *Ernest Hemingway - The Old Man and the Sea*

Chapter 1

Introduction

Ever since microscopes were invented in the 17th century, scientists have been developing increasingly advanced methods to improve their capabilities [1]. These capabilities are no longer solely determined by the hardware such as lenses, but are now predominantly influenced by the software used to control and interpret the hardware results. It is thanks to innovations in the field of super-resolution microscopy during the last few decades that organic material as small as a few nanometers can be observed [2]. New innovations in both the software and the hardware continue to improve the particle localization and tracking capabilities of microscope systems. This chapter introduces the super-resolution microscopy concepts relevant to the topic of this thesis. Section 1-1 offers an explanation on the notion of resolution and the diffraction limit in microscopy. Section 1-2 explains fluorescent microscopy. Having established the resolution of microscopes and the working principles of fluorescence, Section 1-3 introduces super-resolution microscopy. Innovation in the image sensors used in microscopy such as the single-photon avalanche diode (SPAD) are important for this thesis. An overview of image sensors is therefore given in Section 1-4. Section 1-5 gives the motivation behind this thesis and finally, Section 1-6 provides an outline.

1-1   Resolution

Microscopes help us to discover phenomena at a scale that is invisible to the naked eye. An important measure for the quality of a microscope system is its resolution. The resolution is defined as the minimum distance between two objects where they are individually distinguishable. There is a fundamental limit to the resolution known as the diffraction limit. The diffraction limit is a result of the wave nature of light causing it to diffract when passing through a slit (2D) or aperture (3D). This is illustrated in Figure 1-1, which shows the effect of passing point sources through an aperture. The point sources on the right are positioned too close to one another to be distinguishable. Planar light waves coming from the point sources are deformed by the aperture and form a pattern, known as the Airy disk. The Airy disks coming from multiple, nearby, point sources blend together into a single blur, making

it impossible to distinguish the individual point sources. The lenses in a microscope function as an aperture and thus create a hard limit on the resolution of the microscope. The relation between the point source and the image of the point source is called the point spread function (PSF). The PSF is specific to the microscope and contains information about the diffraction limit but also of imperfections in the light trajectory, called aberrations [3].

Ernst Abbe established the mathematical formulation for the diffraction limit of microscopes as $\Delta l = \frac{\lambda}{2\mathrm{NA}}$ [4]. Here, Δl is the spatial resolution of the microscope and λ is the light wavelength. NA is the numerical aperture, defined as $\mathrm{NA} = n_i \cdot \sin(\theta_{\mathrm{half}})$, where n_i is the refractive index of the immersion medium and θ_{half} is the half angle of the microscope. Typically, the numerical aperture does not exceed 1.4 [5]. Visible light has a wavelength around 500 nm. This yields a maximum spatial resolution of $\frac{500}{2 \cdot 1.4} \approx 179$ nm. The optimal spatial resolution of microscopes is therefore between 150 and 250 nm depending on the chosen wavelength and numerical aperture.
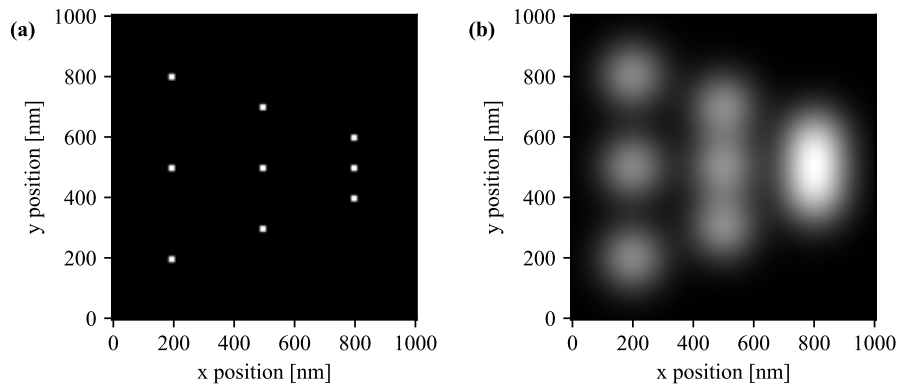
Figure 1-1: Demonstration of the diffraction limit and resolution. **(a)** The true locations of the light point sources. **(b)** The resulting image on the image plane of a microscope. The planar light coming from the light sources is diffracted due to the apertures of the lenses and form Airy disks in the image plane. Beyond a spacing of approximately 200 nm, the point sources become indistinguishable in the image plane. Therefore 200 nm is the spatial resolution of this image.

1-2   Fluorescence Microscopy

Traditional optical microscopes use the scattering, absorption or reflection of light to visualize an object of interest. These methods lack the capability of targeting specific particles within organic samples. Fluorescence provides a solution. Fluorophores absorb light of a specific wavelength and emit light of a different wavelength. Individual, non-fluorescent, molecules of interest can be distinguished by binding them to fluorophores [6]. Connecting different molecules to different color fluorophores allows not only localization of these molecules, but also distinguishing different types through the emitted colors. To understand the concept of fluorescence microscopy the physics of fluorophores and the components are explained below. Total internal reflection fluorescence (TIRF) microscopy was used for the experiments described in this thesis and is therefore also briefly explained.

1-2-1 Fluorophore life cycle

When exposed to a light source of a particular wavelength, fluorophores continuously emit light of a different wavelength. This is called Stokes shift and is crucial for fluorescent microscopes because it allows distinguishing the excitation and emitted light [7]. An example of a fluorophore is Rh6G. Its absorption and emission spectra are shown in Figure 1-2.
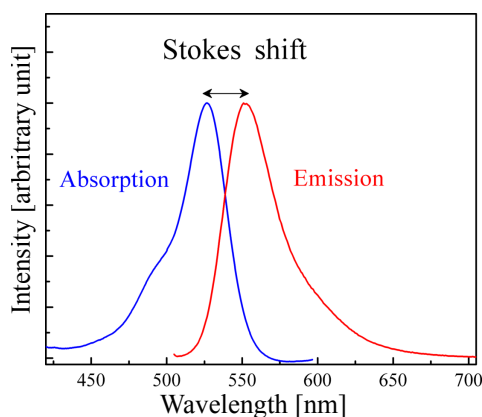
Figure 1-2: Stokes shift demonstrated for the Rh6G fluorophore. When exciting the fluorophore with light of approximately wavelength 520 nm it will emit light with approximately wavelength 570 nm. A fluorescent microscope is capable of only observing the emitted light by passing all the light from the sample through a filter. Source: [8]

To understand the physics behind fluorophores it is important to take a look at the different states a fluorophore can be in. The main process a fluorophore experiences can be described in three steps that are cycled to get a emitting light source:

1. Excitation: a photon from an excitation laser is absorbed by a fluorophore. The fluorophore then goes into an excited singlet state S_1'.

2. Excited-state lifetime: during its excited lifetime (typically nanoseconds) the fluorophore releases energy through heat, thereby going to the relaxed singlet state S_1.

3. Emission: the fluorophore returns to its ground state S_0 and releases a photon while doing this. This typically takes picoseconds. Because of the heat lost during the excited-state lifetime this photon has a longer wavelength (and thus a different color) than the excitation photon.

In reality, the process is more complicated than the three steps described above. Figure 1-3 shows the different states that a molecule can be in. The 'ON' part of the figure is the cycle described above, where the fluorophore emits photons as it alters between the ground state S_0 and the singlet state S_1. However, this does not always happen. In some cycles (about 1 in 1000), the fluorophore does not immediately return to the ground state but goes into the triplet state (T). In even rarer events, the fluorophore goes into the dark (D) or long-lived dark (LLD) states via the triplet state. In these states the fluorophore does not emit any light as it is not performing the above described cycle. The fluorophore is now said to be 'OFF'. After some time the fluorophore goes back to the 'ON' state. This switching between

the 'ON' and 'OFF' states is called blinking, where every blink can have a different duration (usually between a few ms and 100 ms) [9].
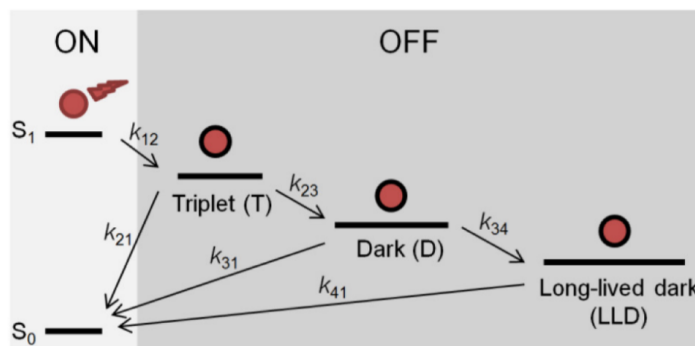
Figure 1-3: A fluorophore is emitting as it gets excited from the ground state S_0 to the excited state S_1 by an impacting photon. At arbitrary times the fluorophore goes into the dark states (T), (D) and (LLD) for a period of time before returning to the ground state. During this time, the fluorophore is not emitting any photons, thereby creating the blinking effect of continuously excited fluorophores. Source: [10]

It can also happen that the fluorophore goes beyond the long-lived dark state and remains there indefinitely. This is called photobleaching. At this point a fluorophore is no longer detectable. The transitions to the different 'OFF' states are dependent on the fluorophore, the excitation wavelength and the excitation power [10].

1-2-2   Fluorescent microscope components

Obtaining a microscopic image using a fluorescence microscope can be explained by following the light trajectory through the setup. Figure 1-4 shows this trajectory. The excitation light comes from a lamp or a laser. An example of an excitation lamp is a high-pressure mercury vapor arc-discharge lamp. Such a lamp has different spectra of light depending on the pressure within the bulb. The excitation intensity can be adjusted by changing the light source [11]. In more recent years, laser and LED light sources have become more customary for fluorescence microscopy. Lasers and LEDs offer a stable light source of a fixed wavelength and intensity. In [12], an overview is provided of what wavelengths to use when exciting different fluorophores, what lifetime can be expected and what laser to use. An excitation filter can be used to filter out any unwanted wavelenghts that are emitted by the laser.

Splitting the excitation light and emitted light is crucial for fluorescence microscopy and is typically done by a dichroic mirror (DM). The DM reflects light of a particular wavelength and allows light of a different wavelength to pass through. In the setup in Figure 1-4 the excitation light is reflected onto the sample and the emitted light is passed through to the detector. The emitted light is only a fraction of the excitation light because of two reasons. First, only part of the excitation light will reach fluorophores that start emitting light. Secondly, these fluorophores emit light to all sides, while only a small cone of this light is captured by the objective. The working of the DM is thus key for fluorescence microscopy because if even a small part of the excitation light reaches the detector it could dominate the signal [11].

Objective lenses are used to focus the excitation light on the sample and to magnify the emitted signal. The magnification and the numerical aperture of the microscope are determined by the objective. The importance of the numerical aperture for the resolution is apparent from Abbes diffraction limit. An objective consists out of one, or multiple lenses [7]. Finally, the light reaches the imager, but not before passing through an emission filter, which filters out any remaining excitation light. The imager could be the researcher's eye, in which case an additional eyepiece lens is required, or a scientific camera. Scientific cameras are discussed at length in Section 1-4.
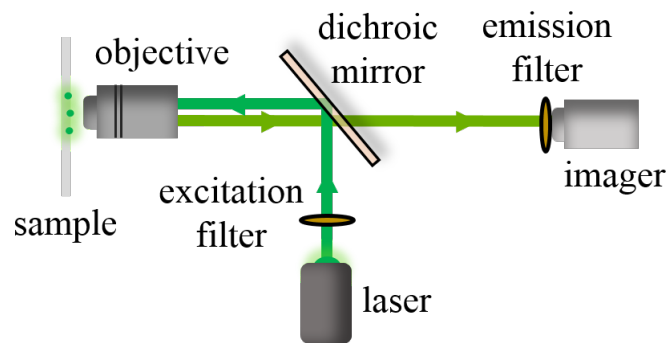
Figure 1-4: The light trajectory in a fluorescence microscope. The light travels from the laser through an excitation filter where unwanted laser wavelenghts are filtered. The dichroic mirror reflects the light onto the sample through the objective. In response, the sample emits light of a different wavelength that gets picked up by the same objective. The dichroic mirror is selected such that it will allow light with the wavelength of the emitted light to pass onto the imager. To filter out any remaining excitation light improperly filtered by the dichroic mirror, an emission filter is placed in front of the imager.

1-2-3   Total internal reflection fluorescence microscope

It is sometimes desired to illuminate a small section of a sample to limit the amount of observed fluorophores. Total internal reflection fluorescence (TIRF) microscopy allows for the excitation of a subset of fluorophores in an aqueous environment near a solid surface [13]. When the light of a laser travelling through a transparent, solid medium with a high refractive index (e.g. glass) hits a medium with a low refractive index (e.g. water), total internal reflection occurs. This happens when the incidence angle θ_1, as calculated in Equation 1-1, is larger than the critical incidence angle θ_c. n_1 and n_2 are the refractive indices of the liquid and solid medium, respectively. As a consequence of the super-critical incidence angle, almost all the light gets reflected back into the solid medium except for the light that moves along the surface of the liquid medium. This light penetrates approximately 100nm into the sample and therefore only excites fluorophores at the surface of the liquid medium [14].

$$\theta_1 = \sin^{-1}\left(\frac{n_1}{n_2}\right) \tag{1-1}$$

The shallow light penetration of TIRF leads to a relatively high signal to noise ratio. Fluorophores that are deeper than 100nm will not be excited and are therefore not observed

by the microscope. The initial motivation for TIRF microscopy was to study the location and dynamics of molecules in a cell membrane close the the substrate. The introduction of variable-angle TIRF, that allows for a user-defined penetration depth, has resulted in more biochemical applications [15, 16]. Figure 1-5 illustrates variable TIRF and shows how fluorophores at different depths are excited more or less depending on the angle of the TIRF microscope.
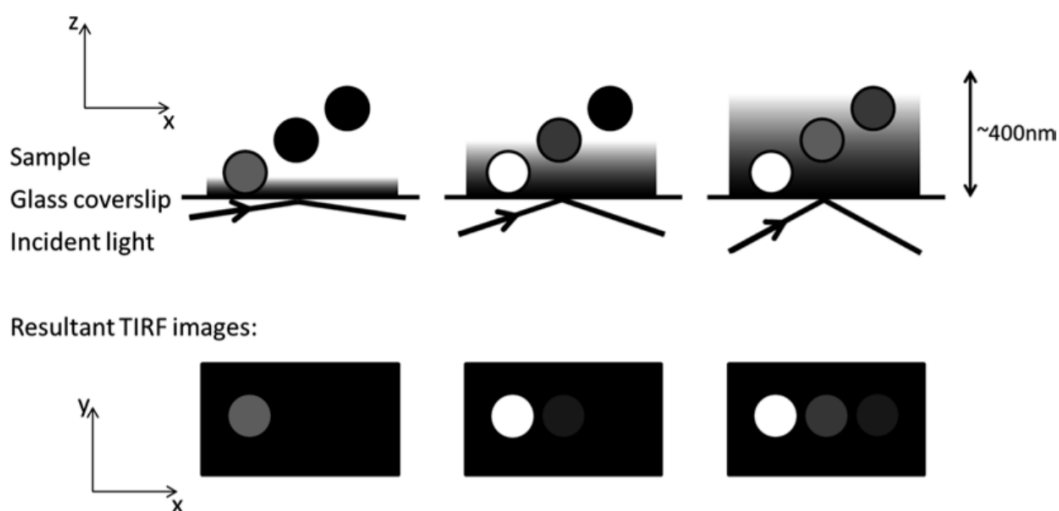
Figure 1-5: Illustration of tuning capabilities of varying-angle TIRF microscopy. Adjusting the incidence angle changes the fraction of light that gets reflected by the liquid medium and the penetration of the excitation light. The emitted light from the fluorophores in the sample is a direct function of the intensity of the excitation light reaching the fluorophores. Source: [16]

1-3 Super-resolution microscopy

In recent years, scientists have found methods to break the diffraction limit and achieve nanometer resolution. Two approaches to super-resolution microscopy are discussed in this thesis: single-molecule localization microscopy (SMLM), and modulation-enhanced SMLM (meSMLM). SMLM is most relevant for this thesis as it is used for the simulations and experiments covered in Chapter 3. Section 1-3-1 describes SMLM methods. meSMLM can benefit from the results of this thesis and is therefore briefly outlined in Section 1-3-2. Since the localization precision is an important metric for super-resolution microscopy, this concept is clarified in Section 1-3-3.

1-3-1 Single-molecule localization microscopy

The principle of SMLM is to circumvent the diffraction limit by ensuring that all particles are at least one diffraction limit removed from one another in a given time instance. This is possible because the point spread function of an individual particle can be used to estimate the position of that particle. Therefore, if each time instance only shows distinguishable fluorophores, all of their positions can be recorded with improved precision over the diffraction

limit. When the recording is continued over multiple time instances, each with a different set of fluorophores, all fluorophore positions are eventually known. All recorded positions can then be combined to visualize a super-resolution image of the region of interest. Previous studies have defined an image formation process to get from sparse emitter data to a super-resolution image [17, 18]. The image processing is discussed at length in Chapter 2.

Having only a subset of the fluorophores emit light at each time instance is essential for SMLM to work. One method to achieve this is point accumulation for imaging in nanoscale topography (PAINT). PAINT targets molecules of interest with freely diffused dyes [19]. The freely diffusing dyes bind to the molecule of interest for a short period of time, during which they can be detected, and are then released again to continue as diffused dyes. Rather than tuning the excitation intensity, the density of fluorophores in the sample is tuned.
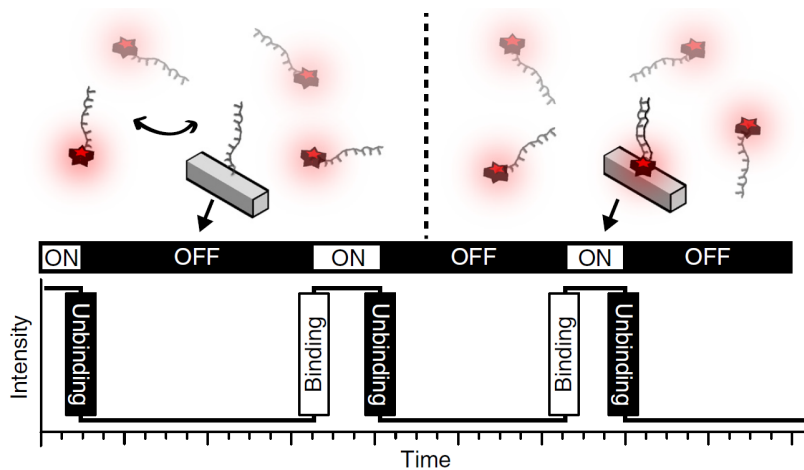
Figure 1-6: Illustratrion of DNA-PAINT. The red stars are docking strands that are attached to a fluorophore. The imaging strand is the gray block, which is in the focal plane. The imaging strand is only visible when a docking strand binds to it. During this period of time the fluorophore is said to be 'ON'. Source: [20]

DNA-PAINT expands on this concept by targeting specific areas of the molecule of interest. This is done by engineering two single-stranded DNA oligomers called the imaging strand and the docking strand. The imaging strand is attached to a fluorescent dye, while the docking strand is attached to a molecule of interest. The imaging strand is diffused and only binds to the docking strand for a limited amount of time. This is illustrated in Figure 1-6. On the left side the docking strands are not attached to the imaging strand, which is therefore not visible. On the right side, one of the docking strands is attached to the imaging strand. During this time the fluorophore can be detected since the imaging system is focused on the location of the targeted molecule. The other imaging strands are diffused and therefore only produce some slight background noise. The duration of the binding and the composition of the strands can be engineered. These characteristics have lead to DNA-PAINT producing the first truly molecular-scale resolution images [20]. A big disadvantage of PAINT and DNA-PAINT is that it can take a very long time for all the docking strands to be connected to an imaging strand for sufficiently long to localize the docking strands [21]. DNA-PAINT is used for the experiments in this thesis.

1-3-2   Modulation-enhanced super-resolution microscopy

Where SMLM uses uniform excitation, modulation-enhanced single molecule localization microscopy (meSMLM) introduces patterned excitation to increase the information content in the emitted signal. SIMFLUX is an example of meSMLM [22]. SIMFLUX illuminates the sample using a sinusoidal wave pattern that alters between three phases and two orientations as shown at the top of Figure 1-7. Similar to SMLM, only a sparse subset of the emitters is activated in each time instance. An imager records the signal resulting from these six different illumination patterns. Summing the photon distributions of the six illumination patterns gives the same emitted photon distribution as when the sample would have been illuminated by a uniform light source. This distribution is commonly assumed to be a Gaussian distribution, where the emitter location is at the center [17]. The sparse subset of emitters is now localized to obtain an initial estimate of the fluorophore locations, as shown on the bottom left of Figure 1-7. Some of the localizations are rejected if the number of photons in the first or last aggregated frame is below a set threshold. Concurrently, the phase, pitch and orientation of the illumination pattern are estimated using a Fourier analysis and by fitting the sinusoidal wave on the detected photon counts. Next, the information of the SMLM processing and the illumination pattern is combined to get an improved location estimate. This gives a higher resolution than SMLM because instead of fitting the photon distribution in a frame with a regular Gaussian distribution, a weighted Gaussian distribution is used. The weights of Gaussian distribution are based on the illumination pattern in that particular frame.
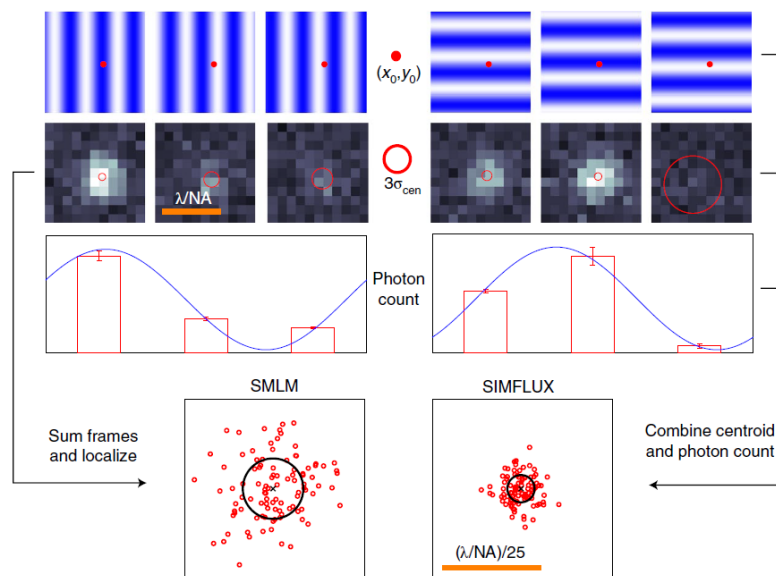

Figure 1-7: Principle of SIMFLUX. First the initial location estimates are found using SMLM. At the same time, the phase and orientation of the illumination pattern is determined using a Fourier analysis. The information about the illumination pattern is then combined with the location estimate to improve the localization precision. Source: [22]

1-3-3 Localization precision

The precision, or uncertainty, of the estimated location is the most important performance indicator for SMLM. Calculating the uncertainty can be done by fitting a Gaussian distribution on the estimated emitter positions for one emitter. The standard deviation σ of the Gaussian distribution is reported as the achieved uncertainty. Different methods exist for determining at what uncertainty two point sources become indistinguishable. One approach is the full width at half maximum (FWHM). If the PSF is assumed to be Gaussian, the FWHM is equal to approximately 2.355σ. This means that two emitters are distinguishable if they are more than one FWHM removed from another.

The Cramér-Rao lower bound (CRLB) gives the lowest possible uncertainty for the location of an emitter. The CRLB is a function of the emitter intensity, the background noise and the emitter position. There are two main applications for the CRLB. First, it allows researchers to predict the resolution of an experiment beforehand. Second, researchers can benchmark a super-resolution method to the theoretical minimum uncertainty, to check if their algorithm is used to its full potential. The CRLB holds for unbiased estimators. Usually, maximum likelihood estimation is used for the localization, which becomes unbiased as the number of observed photons goes to infinity. The CRLB for SMLM is derived in Section 2-4-4.

1-4 Single-photon avalanche diode array

This section briefly touches upon the different types of imagers used in super-resolution microscopy. Next, the single-photon avalanche diode array is introduced as well as details about its imaging modes and noise types.

Currently, two types of photon detectors are most commonly used for imaging in super-resolution microscopy, the electron multiplying charge-coupled devices (EMCCD) and the scientific complementary metal-oxide semiconductor (sCMOS) cameras. Both types of cameras collect light and convert this into a current. This current is then converted to a voltage that can be digitized to obtain an image representing the light intensities over the pixels. The difference between the EMCCD and sCMOS lies in the location of the conversion from current to voltage. In an EMCCD this conversion happens on a chip for all pixels combined. For the sCMOS this happens within the individual pixel [23].

Typically, EMCCD cameras have lower readout noise and higher quantum efficiency than sCMOS cameras [24]. Quantum efficiency (QE) is defined as the photons that get collected as a fraction of the total number of photons that hit the device's light sensitive area. QE is not only dependent on the imaging device, it is also a function of the wavelength. Above or below a particular wavelength the QE can become zero, this wavelength is then said to be outside the band gap [25]. Multiplied by the fill factor the quantum efficiency gives the photon detection efficiency (PDE). The fill factor gives the fraction of the photosensitive area to the total detector area.

There is an uncertainty in the process that converts photons into electrons. This yields excess noise F_n, which is multiplied with the signal to get the noise. F_n is 1 for sCMOS cameras and approximately $\sqrt{2}$ for EMCDD cameras. The simplified signal-to-noise (SNR) ratio for EMCCD cameras and sCMOS cameras is given in Equation 1-2. θ_I is the photon rate from

the emitter, θ_b is the background photon rate per pixel and N_{RO} is the readout noise. [26].

$$SNR = \frac{\theta_I \times QE}{\sqrt{(\theta_I + \theta_b) \times QE \times F_n^2 + N_{RO}^2}} \tag{1-2}$$

In the past two decades the single-photon avalanche diode (SPAD) array was introduced to the field of super-resolution microscopy. SPAD arrays are characterized by their picosecond temporal resolution and are therefore commonly used for time of flight applications [27, 28]. In more recent years, SPAD cameras are used for super-resolution microscopy applications such as SMLM [29, 30], single-molecule tracking [31] and fluorescence-lifetime microscopy [32]. Next to their high temporal resolution, SPAD arrays typically have high frame rates and no readout noise. Downsides include a low fill factor, low quantum efficiency and thus low photon detection efficiency. Additionally, SPAD arrays experience spontaneous avalanches that are not triggered by photons. This type of noise is called dark count rate (DCR) and is discussed in Section 1-4-4.

1-4-1   Working of a single-photon avalanche diode

Each diode in a SPAD array works with a p-n junction capable of detecting light from a wide range of wavelengths. The p-n junction uses the photoelectric effect to convert incoming photons into a current. At a low reverse-bias voltage, this conversion is linear, the diode is then referred to as an avalanche photodiode (APD). However, when the reverse-bias of the p-n junction is larger than the reverse-bias breakdown voltage V_{BD}, the p-n junction triggers a current avalanche for every individual detected photon. This is demonstrated in Figure 1-8b as the step from (1) to (2). This avalanche results in a peak in the measured current and continues until the voltage in the diode drops below the breakdown voltage at point (3). This process is sometimes referred to as the Geiger mode because of the clicking pulses, similar to those of a Geiger counter. The Geiger mode forms the basis of any SPAD. The SPAD is then recharged back to (1) to prepare for the new photon impact. Both during the avalanche and during the recharging the SPAD is insensitive for any photons. This is called the dead time t_{dead} of the SPAD [33]. Figure 1-8a shows that the photons in between the avalanche initiation at (2) and the finished recharging at (3) are not registered. The deadtime is usually between 10 to 100 ns.

There are three ways of dealing with this dead time. *Passive* quenching lets the voltage drop below the breakdown voltage at which point the avalanche stops automatically and the recharging begins. *Active-event driven* quenching detects the photon directly after impact, lowers the bias actively and then recharges directly after the dead time. Finally, *active-clock driven* quenching recharges at set times, irrespective of whether or not an avalanche has occurred [34]. For the remainder of the thesis the active-clock driven quenching is used. The time between two recharges is hereafter referred to as the exposure time t_e.

1-4-2   Binary response

A SPAD outputs a one for one or more photons or zero, for no measured photons during the exposure time of a frame. This exposure time is fixed when using active-clock driven

(a)

(b)
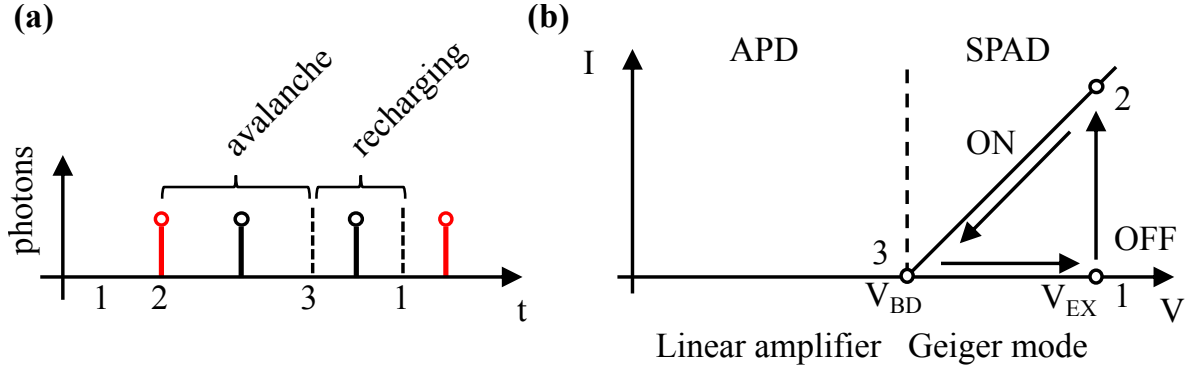
Figure 1-8: Detection cycle of a SPAD. (a) The photon arrivals during a detection cycle of the SPAD. Only the red photons get detected. (b) The voltage and current of the SPAD during its operation cycle. The p-n junction gets reverse-biased beyond the breakdown voltage V_{BD} by excess voltage V_{EX} (point 1). Once a photon triggers the avalanche the current increases and the SPAD is considered 'ON' (point 2). Once the voltage has dropped below the breakdown voltage the SPAD turns 'OFF' (point 3) and needs to be recharged to repeat the cycle. During the avalanche and the recharging period, no photons can be detected, this is referred to as the deadtime.

quenching. Measuring no more than one for one or more photons is a result of the deadtime of the SPAD and is from now on referred to as the binary response of SPAD arrays. Every avalanche is read as a single photon, even if multiple photons reach the pixels during the avalanche and subsequent recharging.

Photons occur in a discrete quantity. For a small amount of photons, this can lead to a difference between the measured and expected number of photons. This is called photon noise and needs to be taken into account when modelling expected photon counts in SMLM applications, where photon counts are low. Photon noise is best described by a Poissonian distribution [35]. If the rate of photon arrivals, or (light) intensity, is given as I, then the probability of observing c photons is given in Equation 1-3, where t_e is the exposure time. The expected number of photons during the exposure time is It_e.

$$\mathbb{P}(C = c) = \frac{(It_e)^c e^{-It_e}}{c!} \tag{1-3}$$

As SPAD arrays can only observe one photon during one exposure time period. Any more photons will get neglected. Using the Poisson distribution, one can calculate the probability of observing one photon as the sum of all probabilities of observing one or more photons. This is given in Equation 1-4. To obtain more contrast in the image, N frames are aggregated. This corresponds to a binomial distribution, since each pixel only has two possible outcomes per exposure time period. Using Equation 1-4b as success probability, Equation 1-5 gives the probability of observing $c^{(N)}$ photons during N exposure time periods.

$$\mathbb{P}(C = 0) = \frac{(It_e)^0 e^{-It_e}}{0!} = e^{-It_e} \tag{1-4a}$$

$$\mathbb{P}(C = 1) = 1 - e^{-It_e} \tag{1-4b}$$

$$\mathbb{P}(C^{(N)} = c^{(N)}) = \binom{N}{c^{(N)}} (1 - e^{-It_e})^{c^{(N)}} e^{-t_e I(N - c^{(N)})} \tag{1-5}$$

1-4-3 Single-photon avalanche diode array

Going from a single SPAD to a 2D array is where the architecture becomes relevant. Ideally, one would put all the pixel electronics in the column underneath the photosensitive part of a pixel. Unfortunately, this is not entirely possible and therefore the fill factor is significantly decreased. This is demonstrated in Figure 1-9, showing the SwissSPAD2, a 512x512 SPAD array with a pixel pitch of 16.4 μm. Only the blue circles in the accentuated area are photosensitive. A SPAD array typically has a fill factor of 5% [36]. This can be mitigated with the use of microlenses that collect the photons of a pixel region and direct them towards the photosensitive area to be measured. Using microlenses, the fill factor can effectively be increased to 50% [37].

In [30], microlenses were applied to a SPAD array for an SMLM application. The improved photon detection efficiency led to a localization precision of 30 nm with only 200 recorded photons in an SMLM image formation process. As a comparison, an EMCCD camera achieved a precision of 15 nm using 1800 photons with a similar approach. 10 times as many photons usually yield a factor $\sqrt{10} = 3.3$ times better precision, but the excess noise F_n of EMCCD cameras lowers this by a factor $\sqrt{2}$.

Figure 1-9 also shows a PCB around the array. This PCB handles the measurement of the avalanches and controls the active time-driven avalanche quenching. The reverse-bias voltage is also controlled by this PCB. The PCB is connect to a field-programmable gated array (FPGA). The FPGA deals with the data rate of SPAD arrays by aggregating multiple frames into one image, storing this image and transferring the data to a computer.

1-4-4 Single-photon avalanche diode specific noise

An important source of noise for the SPAD is the *dark count rate* (DCR) [39]. A dark count occurs when the SPAD discharges and thus records a current, without a photon hitting the photosensitive surface. This is caused by quantum tunneling where a particle has a small probability of moving through a potential barrier without having sufficient energy [40]. The DCR is strongly related to temperature, with lower temperatures leading to less counts per second (cps). This is demonstrated by Figure 1-10, showing the nonnormalized density of pixels with a specific DCR for different temperatures. Figure 1-10 shows a higher DCR per pixel for higher temperatures. For a dark count to occur, there needs to be a dark current and an avalanche needs to be triggered. The probabilities of both these events happening at the same time can be described by a Poisson distribution. The Poisson parameter is a function of device parameters such as the temperature and the excess voltage [41]. A typical SPAD has a DCR of 1-100cps with some SPADs experiencing a much higher DCR up to several thousands CPS [32]. The latter SPADs are referred to as noisy pixels when placed in an array. Because of the differences between SPADs in an array, the DCR is considered pixel-specific.
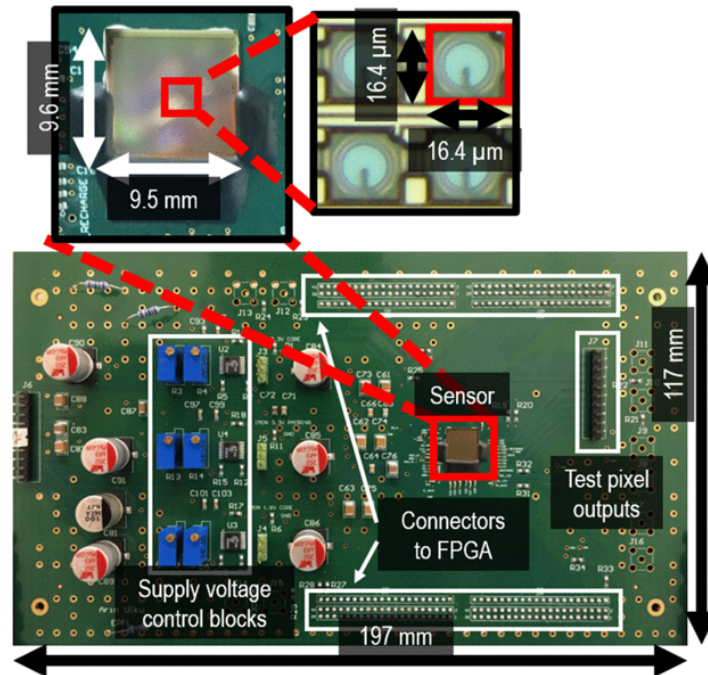
Figure 1-9: The SwissSPAD2 system. The SPAD array, containing 512x512 pixels with pitch 16.4 μm is highlighted. Only the blue part is photosensitive, leading to a low fill factor of 5%. The PCB around the detector measures the avalanches during each exposure time and controls the recharging of the SPADs in the array. TCommonly, this PCB is conntected to an FPGA. This FPGA is programmed to aggregate, store and transmit the frame acquired by the SPAD. Source: [38]
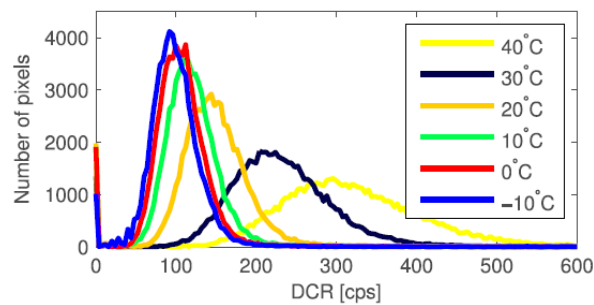
Figure 1-10: Nonnormalized density of the dark count rate for different pixels in the SwissSPAD at different temperatures. There is a strong positive correlation between the temperature of the SPAD and the DCR. Source:[37]

1-5   Thesis motivation

It becomes apparent from Section 1-3-3 that the localization precision is key for the applicability of SMLM methods. The Cramér-Rao lower bound (CRLB) puts a lower limit on the minimum uncertainty that can be achieved in SMLM. The CRLB is dependent on the image formation model. In the derivation of an image formation model, the photon arrivals are assumed to follow a Poissonian distribution [42]. This is valid for cameras that measure photons as a discrete count such as sCMOS and EMCCD cameras. However, as discussed

in Section 1-4-2, this does not hold for cameras that measure a maximum of one photon per pixel during on exposure time, such as SPAD arrays. This binary behavior leads to pixel saturation for high photon fluxes. If multiple pixels in a point spread function get saturated, the Poissonian CRLB no longer puts a reliable lower bound on the achievable uncertainty.

In this thesis, we derive an image formation model and CRLB specifically for the SPAD array. This image formation model takes the binary behavior and frame aggregation of SPAD arrays into account. The binomial image formation model is used to find the binomial maximum likelihood estimation and finally the binomial CRLB. We validate the binomial CRLB using simulations and empirical data. For the empirical data, a TIRF setup with DNA-PAINT is used. Using both the simulated and empirical data, we compare the achieved resolution and the predicted resolution by the Poissonian and Binomial CRLB.

1-6   Outline

This chapter has covered the most important aspects of super-resolution microscopy and of imagers. Chapter 2 discusses the single-molecule localization microscopy image processing in detail. Sections 2-1 to 2-4 deal with the different steps in SMLM, touching upon image pre-processing, position estimation and finally methods for evaluating the results. Chapter 3 is the added value of this thesis. Structured as a paper, Chapter 3 proposes the binomial CRLB and provides simulated and empirical data to validate it. Additionally, Chapter 3 contains supplementary information containing detailed methods and figures. Finally, Chapter 4 summarizes the findings of this thesis and draws conclusions. Chapter 4 also offers a discussion on where this thesis could improve and what future research should be focused on.

<div style="text-align: right">

Chapter 2

</div>

Single-Molecule Localization Microscopy Image Processing

This chapter introduces relevant probability theory to mathematically support the single-molecule localization microscopy (SMLM) image processing discussed in Section 1-3-1. The SMLM image processing serves as the base of the theory presented in Chapter 3 and is shown in Figure 2-1. The most important steps of SMLM image processing are given in process order. First, the acquired images are pre-processed and regions of interest are identified. This is discussed in Sections 2-1 and 2-2. Second, Section 2-3 gives the theory behind the emitter parameter estimation within the regions of interest. Finally, Section 2-4 covers the evaluation of the results, which included post-processing and benchmarking.

2-1   Pre-processing

After recording diffraction limited images in an SMLM setup, the frames need to be pre-processed. In this step, the frames are corrected for the offset and gain of the imaging device. Section 2-1-1 briefly elaborates on gain estimation. For SPAD arrays, multiple images have to be aggregated to create contrast. This is covered in section 2-1-2. A clear mapping of the dark count rate, discussed in Section 1-4-4, is also required for the SPAD array pre-processing.

2-1-1   Offset and gain estimation

The first pre-processing step involves finding the pixel offset caused by the imaging device and correcting for it. Commonly, sCMOS cameras have a fixed offset for every pixel that has to be removed from the acquired image. The offset can be calculated by taking a dark image, for example by leaving the cap on the camera. Additionally, sCMOS cameras apply a gain to their image. The pixel values need to be divided by this gain to get the photon count. The gain can be obtained by collecting images with pixels in different lighting settings. If the gain is defined as g, the intensity is I and the expected photon count for a pixel is $C = gI$, then
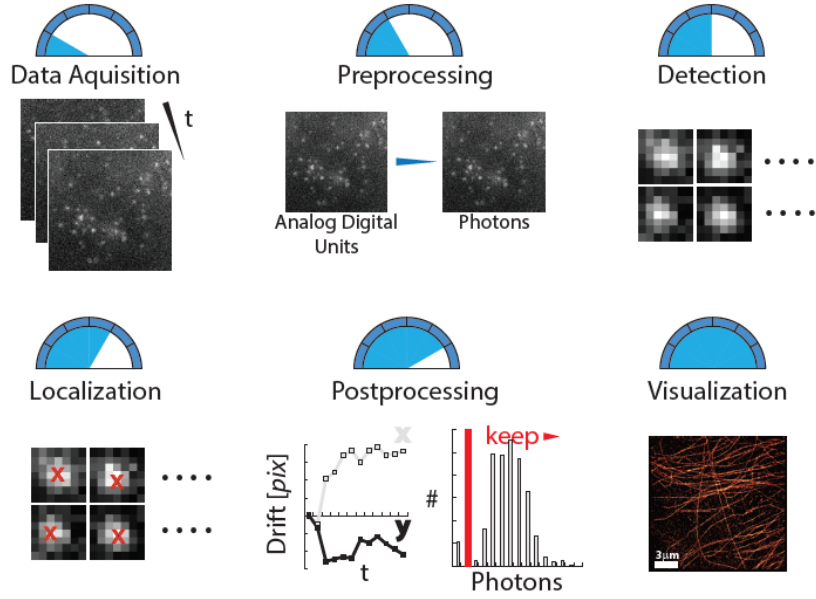
Figure 2-1: The SMLM image formation process. First data is acquired by an imager. This data is pre-processed to get images with a known quantity of photons. Next, regions of interest are detected and the emitter position is estimated. Finally, the localizations are filtered, corrected for drift and visualized. Source: [17]

the variance in the measurements I can be written as $\text{Var}(I) = g^2\text{Var}(C)$. Taking another measurement at intensity $2I$ yields $\text{Var}(2I) = 4g^2\text{Var}(C)$. g can now be calculated from the known variances at the reported intensities as $4g^2 = \frac{\text{Var}(2I)}{\text{Var}(I)}$. As photon counting is an inherently stochastic process, the variances are usually calculated for a set of intensities and a fitted slope is used to find g^2.

2-1-2 Frame aggregation

To obtain contrast in a SPAD array image, N binary frames are aggregated into an image. N, in combination with the exposure time per binary frame, determines the acquisition speed. In general, a low N allows for fast acquisition times, while a high N allows for higher localization precision. This trade-off becomes especially apparent when performing single-molecule tracking. Fast acquisition times means that the tracked particles have moved less between acquired frames, decreasing uncertainty. High acquisition times lead to higher precision for the localization of one molecule. The latter will be extensively discussed in Chapter 3. Figure 2-2 demonstrates the trade-off between the (Brownian) motion of the tracked particles and the acquisition time. The red line shows the motion, which increases linearly for longer acquisition times. The achieved localization precision is plotted by the blue line. The precision initially improves as the imager can acquire more photons during longer acquisition times. For longer acquisition times it becomes equal to the Brownian motion [31].

An advantage of aggregating binary frames versus a fixed exposure time is that the images can be sized and spaced optimally. Once a rough estimate of the molecule location is known, the frames can be aggregated such that only the 'ON' time of a molecule is within an image.

This is called smart-aggregation [29]. Smart-aggregation maximizes the SNR in this manner. This is demonstrated with a simulation in Figure 2-3 and compared to an EMCCD imager, which has no aggregation freedom. It can be observed that image (ii) and (iii) of the EMCCD images contain some of the 'ON' time of the molecule, but both contain less total intensity than the single 'ON' image of the smart aggregated SPAD array.
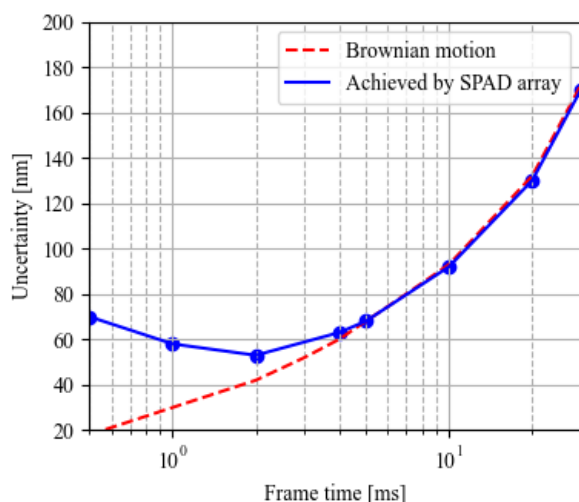
Figure 2-2: Localization uncertainty achieved by SPAD during single-particle tracking. The RMSD follows the Brownian motion for large frame time but has a higher RMSD when the frame time is limited. Source: adapted from [31]
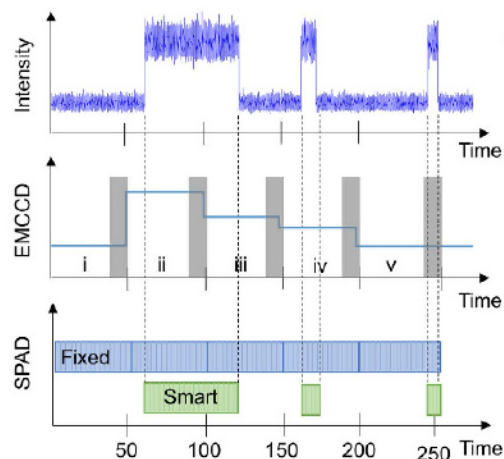
Figure 2-3: SPAD smart aggregation scheme in comparison to a regular SPAD array and an EMCCD. Only the frames of one blink are summed to identify the emitter location. Smart-aggregation can lead to a higher SNR than an EMCCD or sCMOS could achieve. Source: [29]

2-1-3 Single-photon avalanche diode noise

SPAD arrays do not have offset or a gain as they only output a one whenever a pixel has measured one or more photons. SPAD arrays do have DCR that needs to be taken into account during parameter estimation. The average DCR in each pixel can be recorded in a dark setting, for example when the cap is left on. When detecting regions of interest, or estimating the emitter position, the pixel-dependent DCR is subtracted from the acquired data.

2-2 Spot detection

The first step in the estimation process is finding the regions that likely contain an emitter for each time instance. Figure 2-4a shows the diffraction limited image that one might observe in a microscope where all molecules are emitting simultaneously, As discussed in Section 1-3-1, using DNA-PAINT, Figure 2-4a can be split into a number of images with distinguishable emitters. This is shown in Figure 2-4b.

For each image in Figure 2-4b, individual spots are detected and the area around them is defined as a region of interest (ROI). This is sometimes also referred to as segmentation. These ROIs are then used as the input to the parameter estimation. The ROI size is commonly a function of the size of the expected standard deviation of the point spread function of the microscope σ. For this thesis the ROI size is calculated as $4 + 2(\sigma + 1)$ [22]. There are a few established spot detection methods.

Spot detection can be as simple as using an intensity threshold. Any pixel with an intensity above the set threshold forms the center of an ROI [18]. A slightly more advanced method that was used for this thesis involves two-step filtering and then applying an intensity threshold. First, two images are created by applying a uniform filter of two different sizes to the raw image. These two images are then subtracted from one another and local maxima within regions of about half the predetermined ROI size are calculated. Any local maximum with an intensity above a pre-determined threshold is accepted as the center of an ROI [22].

Finding a suitable threshold is an iterative process. It is usually the mean pixel value multiplied with a certain factor. This factor is tuned until a satisfactory amount of the expected number of molecules is detected and the number of invalid ROIs (those containing noise, or noisy pixels) is limited.

(a)   **(b)**   **(c)**
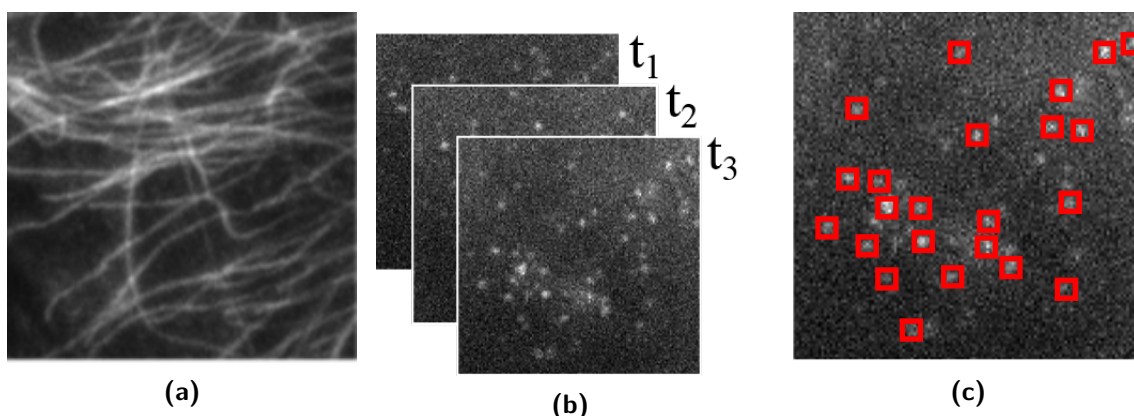
Figure 2-4: Dividing a diffraction limited image into multiple time instances. **(a)** A diffraction limited image that is split up into a number of images obtained at different times t_1, t_2 and t_3. **(b)** The individual emitters are now distinguishable for the different time instances and can be individually localized. **(c)** ROIs are detected. These ROIs are used as input to the parameter estimation algorithm. Source: adapted from [17]

2-3   Parameter estimation

During this step, the emitter's position and intensity are estimated. This estimation requires an image formation model, an estimation method and an optimization algorithm.

2-3-1   Image formation model

To get a good estimate of the emitter position it is important to have a mathematical model of the emitter and any noise sources, this is called the image formation model. Using the

image formation model, we can get an expected photon rate $\mu(x_k, y_k, \theta)$ in a pixel k and a distribution of the photon count C_k. Hereafter, $\mu(x_k, y_k, \theta)$ is referred to as μ_k. μ_k is a function of the pixel location $[x_k, y_k]$ and the vector θ, given in Equation (2-1). Here, the emitter position in the image is given as the coordinates θ_x and θ_y. The intensity is θ_I in photons $\cdot s^{-1} \cdot m^{-2}$ and θ_b is the background noise in photons$\cdot s^{-1} \cdot$px^{-1}. A detailed derivation of μ_k can be found in Appendix A.

$$\theta = \begin{bmatrix} \theta_x & \theta_y & \theta_I & \theta_b \end{bmatrix} \tag{2-1}$$

The photon rate μ_k is determined by the sum of the photons from the emitter and from the background. This is shown in Equation 2-2, where $h(x-\theta_x, y-\theta_y)$ is the emitter point spread function (PSF) and $[\Delta x, \Delta y]$ gives the pixel size. In Equation 2-2 the PSF is integrated over a pixel to account for the discrete nature of the imager pixels. The background θ_b is defined as photon rate per pixel and is therefore already discretized. If we assume the emitter PSF to have a Gaussian shape, $h(x, y)$ is given in Equation 2-3 [17], where σ is the PSF standard deviation.

$$\mu_k = \theta_I \int_{y_k - \frac{\Delta y}{2}}^{y_k + \frac{\Delta y}{2}} \int_{x_k - \frac{\Delta x}{2}}^{x_k + \frac{\Delta x}{2}} h(x - \theta_x, y - \theta_y)^2 dx dy + \theta_b \tag{2-2}$$

$$h(x, y)^2 = \frac{1}{2\pi\sigma^2} e^{\frac{-x^2 - y^2}{2\sigma^2}} \tag{2-3}$$

The next step is to implement the photon noise into the noise model. Similar to Section 1-4-2, the probability of observing a number of photons is determined by the Poissonian distribution. μ_k is the rate of photon arrivals and the exposure time t_e is multiplied with the rate to obtain the expected number of photons per frame. This yields the probability distribution as given in Equation 2-4, where c_k is the photon count in a pixel k. The photon rate is identical for a SPAD array, but the probabilities are based on a binomial distribution as described in Equation 1-5. An extensive derivation of these probabilities is given in the Supplemental Document of the Manuscript in Chapter 3.

$$\mathbb{P}(C_k = c_k) = \frac{(\mu_k t_e)^{c_k} e^{-\mu_k t_e}}{c_k!} \tag{2-4}$$

2-3-2   Maximum likelihood estimation

Now that an image formation model is defined, the optimal parameters for an emitter within an ROI need to be found. The parameters that are estimated are $\theta = [\theta_x, \theta_y, \theta_I, \theta_b]$. For this estimation, maximum likelihood estimation (MLE) or nonlinear least squares is commonly used. As previous research has shown that maximum likelihood yields more precise results it will be used for this thesis [43]. MLE becomes unbiased and minimum variance as the number of observations goes to infinity [44]. In practice for SMLM, this happens for more than 100 observed photons [42].

The likelihood $L(\theta|x)$ is calculated as the probability that the given set of i.i.d. observed photon counts $c = [c_1, c_2, \ldots, c_n]$ was found with a given set of parameters θ. The set of

observations are the measured photon counts for all n pixels within the ROI. The likelihood of observing a certain set of pixel counts is given in Equation 2-5.

$$L(\theta|c) = \prod_{k}^{n} \frac{\mu_k(x,y)^{c_k} e^{-\mu_k(x,y)}}{c_k!} \tag{2-5}$$

2-3-3 Optimization algorithm

Maximizing the likelihood is a time sensitive process and therefore benefits from a fast algorithm. For this thesis the Levenberg-Marquardt algorithm is used. The Levenberg-Marquardt algorithm is derived from the Newton-Rhapson algorithm. The Newton-Rhapson algorithm is designed to find the roots of the cost function and it requires the derivative of the cost function. Since the goal of SMLM is to find the maximum likelihood, the roots of the derivative are searched. This means that the gradient and Hessian of the cost function are required, such that the algorithm becomes Equation 2-6, where θ is the unknown parameter vector, $J(\theta)$ is the gradient vector, i is the iteration and $H(\theta)$ is the Hessian.

$$\theta_{i+1} = \theta_i - J(\theta_i)H(\theta_i)^{-1} \tag{2-6}$$

The Newton-Rhapson algorithm tends to fail when one of the gradients encounters a stationary, or nearly stationary, point, i.e. the Hessian is (almost) singular. When this happens the algorithm becomes unstable or terminates due to division by zero. The Levenberg-Marquardt algorithm fixes this by adding a damping term λ_{LM} to the Hessian. For large damping terms, the Levenberg-Marquardt parameter simplifies to a gradient descent method, while taking a small damping term gives the convergence of the Newton-Rhapson method. Equation 2-7 gives the Levenberg-Marquardt algorithm.

$$\theta_{i+1} = \theta_i - J(\theta_i)(H(\theta_i) + \lambda_{LM}I)^{-1} \tag{2-7}$$

Since MLE is a non-convex problem in SMLM, there is no guarantee that the maximum is found. The initial condition is thus important. For this thesis, a centre-of-mass calculation is used to get an initial estimate for the position within the ROI. The intensity and background intensity are initialized using the sum of the photon count and the mean photon count, respectively. Alternatively, when it is critical that the global optimum is found, a multi-start algorithm could be used.

2-4 Post-processing

The first step of post-processing is to filter out localizations that do not represent an emitter. The χ^2-test or Kolmogorov-Smirnov test can be applied for this. Next, any drift that occurred during data acquisition has to be removed. After this, the localization uncertainty is calculated using the standard deviation of the different estimates of one emitter's position. Finally, to benchmark the estimation algorithm, this uncertainty can be compared to the Cramér-Rao lower bound.

2-4-1 Drift correction

During the acquisition of the camera the sample can drift slightly, which spoils the precision of the localizations. This drift can be corrected during the post-processing of the estimated positions. A common approach for this is redundancy cross correlation (RCC) drift correction [45]. For this method, the cross-correlation between binned images is calculated. Each image contains a sparse subset of all molecules due to the blinking and are therefore binned. There have to be enough localizations in each bin. Next, the bins are shifted with respect to one another such that the cross-correlation is maximized. The shift that yields the maximum cross-correlation corresponds to the optimal drift correction for that time instance.

2-4-2 χ^2-test

The χ^2-test is used to quantify the difference between the expected photon counts and the measured photon counts within an ROI. The χ^2 statistic is given in Equation 2-8. Using the probability distribution given in Equation 2-4, the expected value and standard deviation can be calculated for the χ^2-statistic. Estimates with a χ^2-statistic of more than the expected value plus two standard deviations are removed from the results. The expected value and standard deviation of the χ^2-statistic are given in Equations 2-9 and 2-10, respectively. A derivation of Equations 2-9 and 2-10 is given in Appendix B.

$$\chi^2 = \sum_k^n \frac{(c_k - \mathbb{E}[c_k])^2}{\mathbb{E}[c_k]} = \sum_k^n \frac{(c_k - \mu_k(x_k, y_k)t_e)^2}{\mu_k(x_k, y_k)t_e} \tag{2-8}$$

$$\mathbb{E}[\chi^2] = n \tag{2-9}$$

$$\sigma^2[\chi^2] = \sum_k^n \frac{1}{\mu_k(x_k, y_k)t_e} + 2n \tag{2-10}$$

2-4-3 Kolmogorov-Smirnov test

The Kolmogorov-Smirnov (KS) test is another method to assess the quality of an estimate. The test is based on the KS statistic, which can be converted into a type 1 error rate for continuous distributions. The KS statistic of an estimate is calculated by taking the maximum distance between the sorted observed pixel values and the sorted expected pixel values. The sorted data sets are normalized. Mathematically, this is described in Equation 2-11, where T_{KS} is the KS statistic and n is the number of pixels. F_{obs} and F_{exp} are the sorted and normalized pixel values of the observed and expected data set, respectively. [44]. Calculating the KS statistic is illustrated in Figure 2-5, showing a simulation of F_{obs} and F_{exp}. As the image formation model is based on a discrete distribution, namely Poissonian for sCMOS cameras and binomial for SPAD arrays, the KS statistic can not be converted into a type 1 error. However, it is possible to benchmark two proposed image formation models by comparing the KS statistic for a number of scenarios to benchmark both models with respect to one another [46].

$$T_{KS} = \sup_{a \in n} |F_{\text{obs}}(a) - F_{\text{exp}}(a)| \tag{2-11}$$
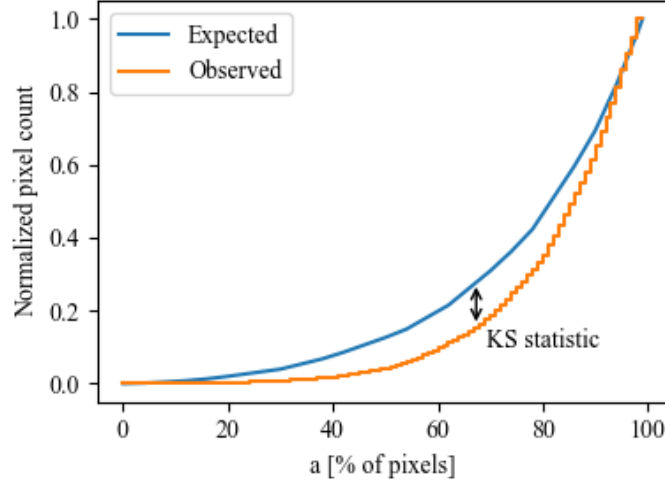
Figure 2-5: Demonstration of the KS statistic for an estimate. The steps are the normalized cumulative observed pixel counts while the continuous line represents the normalized cumulative expected pixel counts given the estimated parameters. The maximum distance between both lines represents the KS statistic.

2-4-4   Cramér-Rao lower bound

The CRLB was introduced in Section 1-3-3 and is the last step of the SMLM image formation process. It is calculated in Equation 2-12, where the denominator is commonly known as the Fisher information for this scalar case and the Fisher information matrix for the vector variant [47]. For the CRLB to hold, the likelihood has to satisfy Leibniz' integral rule. This can be extended to a vector of parameters, as is the case when applying the CRLB to SMLM. The Fisher information matrix is then defined as Equation 2-13 [42]. For the derivation of the CRLB, the reader is directed to Chapter 4 of [47].

$$Var(\hat{\theta}) \geq \frac{1}{-\mathbb{E}\left[\frac{\partial^2 l(\theta|c)}{\partial \theta^2}\right]} = \text{CRLB}(\theta) \tag{2-12}$$

$$I_{ij}(\theta) = \mathbb{E}\left[\frac{\partial \ln(L(\theta|c)}{\partial \theta_i} \frac{\partial \ln(L(\theta|c))}{\partial \theta_j}\right] \tag{2-13}$$

Combining the likelihood function in Equation 2-5 with the definition of the Fisher information matrix in Equation 2-13 gives the Fisher information matrix in Equation 2-14 [42]. Again, c_k is the observed photon counts and μ_k is the expected photon rate from the estimated parameters for pixel k and t_e is the exposure time. This means that $E[(c_k - \mu_k t_e))^2]$ is the variance of the Poissonian process. The variance of a Poissonian process is equal to

its expected value, therefore Equation 2-14 can be rewritten to Equation 2-15. The partial derivatives required to solve Equation 2-15 are given in Appendix A.

$$I_{ij}(\theta) = \mathbb{E}\left[\sum_k (c_k - \mu_k t_e)^2 \frac{1}{\mu_k^2} \frac{\partial \mu_k}{\partial \theta_i} \frac{\partial \mu_k}{\partial \theta_j}\right] \tag{2-14}$$

$$I_{ij}(\theta) = \sum_k \frac{1}{\mu_k} \frac{\partial \mu_k}{\partial \theta_i} \frac{\partial \mu_k}{\partial \theta_j} \tag{2-15}$$

Chapter 3

Manuscript

This chapter presents the findings of this thesis structured as a paper. Additionally, detailed information about the methods and results can be found in the supplementary information.

Theoretical Minimum Uncertainty of Single-Molecule Localizations Using a Single-Photon Avalanche Diode Array

Quint Houwink,[1] Dylan Kalisvaart,[1] Shih-Te Hung,[1] Jelmer Cnossen,[1] Daniel Fan,[1] Paul Mos,[2] Arin Can Ülkü,[2] Edoardo Charbon,[2] and Carlas Smith[1,*]

[1]*Delft Center for Systems and Control, Delft University of Technology, Delft, the Netherlands*
[2]*Advanced Quantum Architecture Lab, EPFL, Neuchâtel, Switzerland*
[*]*c.s.smith@tudelft.nl*

Abstract: Single-photon avalanche diode (SPAD) arrays can be used for single-molecule localization microscopy (SMLM) because of their high frame rate and lack of readout noise. SPAD arrays have a binary frame output, which means photon arrivals should be described as a binomial process rather than a Poissonian process. Consequentially, the theoretical minimum uncertainty of the localizations is not accurately predicted by the Poissonian Cramér-Rao lower bound (CRLB). Here, we derive a binomial CRLB and benchmark it using simulated and experimental data. We show that if the expected photon count is larger than one for all pixels within one standard deviation of a Gaussian point spread function, the binomial CRLB gives a 46% higher theoretical uncertainty than the Poissonian CRLB. For typical SMLM photon fluxes, where no saturation occurs, the binomial CRLB predicts the same uncertainty as the Poissonian CRLB. Therefore, the binomial CRLB can be used to predict and benchmark localization uncertainty for SMLM with SPAD arrays for all practical emitter intensities.

1. Introduction

Single-photon avalanche diode (SPAD) arrays are image detectors capable of detecting single photons at a rate of 100 kfps [1]. SPAD arrays are used for single-molecule localization microscopy (SMLM) [2–4], single-molecule tracking [5], and fluorescence lifetime imaging microscopy (FLIM) [6, 7]. SPAD arrays lack readout noise, giving them an advantage over sCMOS cameras. Individual SPADs are also able to time-stamp photons with picosecond precision, which makes them viable options for time-of-flight (ToF) imaging [8, 9].

A key feature of a SPAD array is its output of binary frames. A number of frames are aggregated into an image to create contrast. The binary output is because SPADs work with a reverse-biased p-n junction that is ultra-sensitive to incident photons. A photon triggers an avalanche in the junction causing a current that can be measured. After the avalanche, the SPAD has to recharge beyond its breakdown voltage. During this recharging the SPAD is insensitive to incident photons as shown in Figure (1b). Some SPADs are capable of measuring photons during recharging, but this requires the SPAD to store the counts in a pixel memory, which lowers the fill factor of a SPAD array. Therefore, we focus on SPADs that measure one photon maximum per detection cycle, giving a binary output. [10].

A fundamental problem in SMLM is determining and achieving the optimal precision with which single molecules are localized. The theoretical minimum uncertainty can be calculated using the Cramér-Rao lower bound (CRLB). The CRLB holds for an unbiased parameter estimation problem such as maximum likelihood estimation (MLE), which is asymptotically unbiased [11]. The CRLB is dependent on the image formation model. In the derivation of an image model for

SMLM with negligible readout noise, the photon count is modelled as a Poissonian process [12]. The Poissonian process accounts for the discrete nature of photon arrivals.

Using a Poissonian distribution for calculating the CRLB for SMLM with a SPAD array is inaccurate as the SPAD array is unable to register more than one photon per exposure time period. Therefore, if saturation occurs, there is no guarantee that the CRLB derived by [11] holds for experiments using a SPAD array. Where saturation is defined as all pixels within one standard deviation of a point spread function having more than one expected photon per frame. Research into performing SMLM with SPAD arrays [2, 5, 13] has refrained from using a CRLB. Therefore, applied SMLM methods cannot be benchmarked to a theoretical minimum uncertainty.

Here, we derive the CRLB for SMLM applications when using a SPAD array. The output of the SPAD array is modelled as a binomial distribution, thereby creating a physically accurate representation of aggregating multiple binary SPAD array images. We validate this model using simulations and empirical data. In these experiments we show that, if saturation occurs, the binomial CRLB gives a higher theoretical uncertainty than the Poissonian CRLB. Without saturation, the binomial CRLB predicts the same uncertainty as the Poissonian CRLB.

2. Methods and data

2.1. Maximum likelihood estimation for single-photon avalanche diode array

We use maximum likelihood to obtain an estimate of the molecule position. For the derivation of the image formation model needed to calculate the likelihood, molecules are assumed to be excited by a uniform laser light and have a Gaussian point spread function [14]. This point spread function is summed with any background noise and discretized over the finite size of the pixels of the SPAD. This yields the photon rate $\mu_k(\theta)$ in pixel k. θ is the parameter vector containing the emitter position, intensity, and the background intensity. $\mu_k(\theta)$ is thereafter referred to as μ_k. To account for the discrete nature of light, the photon arrivals are modelled as a Poissonian process with a rate equal to the expected photon count. This does not yet take the binary behavior of the SPAD or SPAD particular noise into account.

The dark count rate (DCR) is a noise that is particular to SPADs. The DCR is caused by spontaneous avalanches within the SPAD and can be modelled as a Poissonian process over time [15]. As some SPADs in the array are highly vulnerable to DCR (10-100 times higher than the median DCR), the DCR is pixel-dependent. DCR_k is considered to be known for each pixel k (see Supplementary Figure (S3) and (S4)). Summing the DCR with the incident photon rate yields the expected photon rate. Equation (1) shows the probability mass function of the photon detections if the SPAD output would be discrete. Here, c_k is the photon count in pixel k and t_e is the exposure time.

$$\mathbb{P}(C_k = c_k) = \frac{t_e \left(\mu_k + DCR_k\right)^{c_k} e^{-t_e(\mu_k + DCR_k)}}{c_k!} \tag{1}$$

The SPAD has a binary output, therefore we sum the probabilities of observing more than zero photons in one frame to get the probability of observing one photon. This probability is equal to one minus the Poissonian probability of observing zero photons, i.e. $c_k = 0$. This transforms the Poissonian distribution into a Bernoulli distribution. The photon arrivals in a pixel thus follow a binomial distribution when aggregating multiple binary frames. The likelihood of an observed image $\vec{x}$ with n pixels is computed in Equation (2), where $c_k^{(N)}$ is the number of photons in pixel k, upon aggregating N frames. It is assumed that there is no correlation between pixels, i.e. no crosstalk [16]. Equation (2) can be maximized to obtain a parameter estimate. We use the Levenberg-Marquardt algorithm to maximize the likelihood (see Supplementary Note (S1)).

$$L(\theta|\vec{x}) = \prod_{k=1}^{n} \binom{N}{c_k^{(N)}} (1 - e^{-t_e(\mu_k + DCR_k)}) c_k^{(N)} e^{-t_e(\mu_k + DCR_k)(N - c_k^{(N)})} \tag{2}$$

2.2. Cramér-Rao lower bound for single-photon avalanche diode array

The CRLB gives the lowest possible uncertainty of the position of a molecule [11]. There are two main applications for the CRLB. First, it provides a bound on the achievable resolution of an experiment beforehand. Second, it can be used to benchmark a particular localization approach. The CRLB holds for unbiased estimators and is defined as the entries on the diagonal, i.e. $i = j$, of the inverse of the Fisher information matrix [17]. Using the likelihood function in Equation (2), the Fisher information matrix for the binomial CRLB is calculated. (see Supplementary Note (S2)).

$$\text{CRLB}(\theta) = \left[Nt_e^2 \sum_{k=1}^{n} \left(\frac{\partial \mu_k}{\partial \theta_i} \frac{\partial \mu_k}{\partial \theta_j} \frac{e^{-t_e(\mu_k + DCR_k)}}{1 - e^{-t_e(\mu_k + DCR_k)}} \right) \right]^{-1} \tag{3}$$

2.3. Simulation method

We performed simulations of emitter imaging at intensities where no saturation occurs (all pixels have less than 1 expected photon per pixel) up to the point where heavy saturation occurs (4 expected photons for the center pixels). This gives a broader scope of the behavior of the achieved and theoretical uncertainty when acquiring SMLM images using a SPAD array. Blinking behavior of the emitters was neglected to have a constant intensity over the localizations. The background intensity was kept constant for each frame in one simulation and at 3% of the emitter intensity in another simulation.

The simulated frames are obtained using a Gaussian distribution for the point spread function of a single emitter. The point spread function is given a standard deviation of 102 nm, which is equal to the point spread function of the diffraction limited experimental setup. The intensity is varied over a range of photon counts, from 90 to 22,000 photons per image. DCR is simulated using experimental SwissSPAD2 data acquired in a dark environment. Each frame is made binary by first applying a Poissonian distribution on the calculated intensity for a pixel and then setting all pixels with a value above one to one. Subsequently, N frames were aggregated to get an image with a total exposure time of $N \times t_e$.

Maximum likelihood estimation described in Section 2.1 estimates the optimal position and intensity of the emitter, as well as the background intensity. Each intensity simulation is repeated 500 times. A Gaussian distribution is fitted on the x-value and y-value of the estimated positions to obtain the mean position and its standard deviation σ_x and σ_y.

2.4. Empirical method

An experimental setup was built to validate the proposed CRLB model. The used SPAD array is the SwissSPAD2, shown in Figure (1c). The SwissSPAD2 has an array of 512x256 pixels with a pitch of 16.38 μm. It has a photon detection probability of 35% and a fill factor of 10.5% [18]. The fill factor is increased to approximately 50% for this experiment through the use of microlenses. For this experiment the SwissSPAD2 is operated at an excess bias of 6.5V.

The SMLM setup used is a total internal reflection fluorescence (TIRF) microscope. A diagram of the setup is shown in Figure (1a). A 200 mW, 532 nm continuous-wave laser (Optoelelectronics Tech. PSU-H-LED) is collimated and directed to a 60x objective (Olympus Apo N 60x/1.49Oil) where it arrives off-center such that the light is deflected along the surface of the sample. The beam
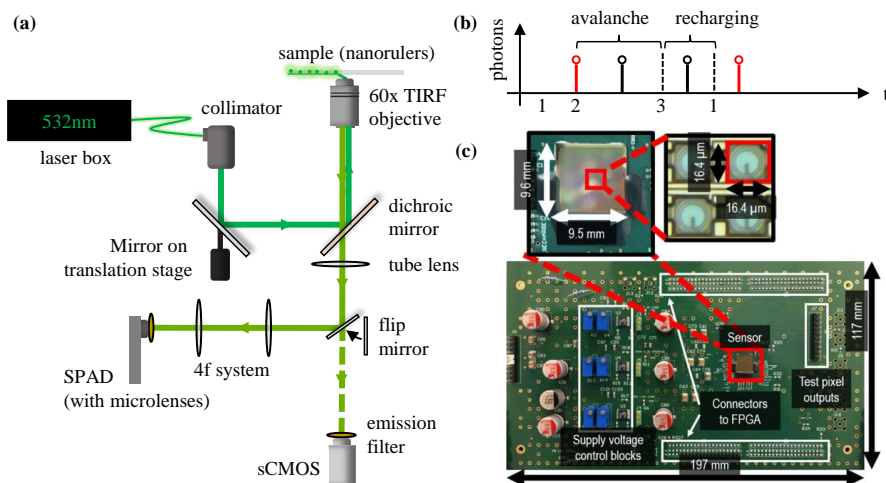
Fig. 1. Experimental method for single-molecule localization using a SPAD array. (**a**) The TIRF setup used for the experimental data in this paper. A green laser (532 nm) is directed towards an objective such that it enters the sample at a critical angle, only exciting the nanorulers close to the coverslip. The emitted light is filtered from the excitation light using a dichroic mirror and magnified 2.7x by a 4f system before being focused on the 512x256 SPAD array using microlenses. An sCMOS camera was used to find the focal plane and for imaging comparison. (**b**) A schematic of photon arrivals on the SPAD. The SPAD is charged beyond its breakdown voltage at 1. An incident photon at 2 then triggers an avalanche. The SPAD is then recharged at point 3. No photons are detected between 2 and 1, causing the binary behavior of the SPAD. (**c**) The SwissSPAD2, consisting of 256x512 pixels. The pixels have a pitch of 16.38μm, and a low fill factor of 10.5% that was increased to 50% using microlenses.

can be moved further from or closer to the center using a mirror and a lens on a translation stage. This causes only a fraction of the fluorophores, i.e. those close to the coverslip, to emit photons, reducing the background noise. A dichroic mirror (Semrock, Di01-R405/488/532/635-25x36) filters the emitted light from the sample prior to the tube lens (ThorLabs, AC508-180-AL-M). A flip mirror (ThorLabs, TRF90/M) switches between an sCMOS camera (ANDOR Zyla 4.2) for comparison and the SwissSPAD2. As the sCMOS camera has a pixel pitch of 6.5μm, a 4f system (ThorLabs, AC508-075-AL-M and AC508-200-AL-M) with magnification 2.7x is added to the SPAD trajectory to have a point spread function on the SPAD array of similar size to that imaged by the sCMOS. A quadband filter (Semrock, 390/482/532/640 HC) on the imagers filter the remaining excitation light. DNA-Paint nanorulers (Gattaquant PAINT 80RG) are used as the sample. The nanorulers consist of three binding sites seperated linearly by 80 nm between each site. Fluorophores (ATTO542 and ATTO655) connect to the binding sites for a varying amount of time until releasing again. This results in blinking and thus sparse emitters which are capable of being localized using SMLM algorithms. The 532 nm laser source excites only the ATTO542 fluorophores, which emit light of wavelength 562 nm. At this wavelenght the SwissSPAD2 is most sensitive for incident photons (see Supplementary Figure (S7)).

Experimental data is gathered for a range of aggregated frames and exposure times, keeping the total exposure time per image constant at 31 ms for the SPAD array. At this total exposure time the expected number of photons per image is approximately 1000. N ranges from 16 to 2048 frames. For every N, a set of dark images is acquired to register the DCR and a set of TIRF images is collected for localization. Regions of interest (ROIs) are identified in each image by

placing a threshold on a Gaussian ($\sigma = \sigma_{PSF}$) filtered image [19]. Estimates are then obtained by maximizing the likelihood given in Equation (2). Many estimates do not represent an emitter, but dust on the sample or a cluster of hot pixels. To filter these estimates, the χ^2 value was calculated for an estimate and filtered above a threshold (see Supplementary Note 1). Any drift in the estimates is removed using redundancy cross-correlation [20]. Finally, the estimates are clustered when they are within three times the expected uncertainty from one another and not more than five frames apart [12]. Each cluster is fit with a Gaussian distribution. The mean and standard deviation of the fitted distribution yield the final emitter position and uncertainty, respectively.

3. Results

3.1. Simulated results

An emitter was simulated at 25 intensities, equidistantly spaced within $[10^2, 10^4]$ photons per image. This was repeated for 255, 510 and 1275 aggregated frames per image. Figure (2) shows the achieved uncertainty for the localization of this emitter as well as the theorized minimum uncertainty calculated using the binomial and Poissonian CRLB. The intensity range was selected such that a distinction can be made between the uncertainty theorized by both CRLB models. Figure (2a) shows a constant background rate of 2.5 photons per pixel in each frame. At this rate, almost no saturation occurs, which causes the binomial and Poissonian CRLB to be overlapping for almost all intensities. The CRLB models start deviating notably at emitter intensities above 4000 photons per image, as is shown in the zoom in Figure (2b). In this plot it becomes clear that the localization algorithm on the simulated images achieves the same uncertainty as the binomial CRLB.

An additional simulation was performed while keeping the background intensity at 3% of the emitter intensity. The Poissonian CRLB is now identical for all aggregation numbers. It can be observed that the background contributes to the saturation and the difference between the CRLB models is apparent at more than 2000 emitter photons per image. The vertical lines indicate the point where saturation occurs for the different aggregation numbers. The theoretical minimum uncertainty of the binomial CRLB is 46% higher than the theoretical minimum uncertainty of the Poissonian model when saturation occurs. There is a fivefold difference between the binomial CRLB and Poissonian CRLB, for the maximum simulated intensity of 20000 emitter photons per image. This occurs when there is heavy saturation in the simulated image due to more than five expected photons in the center pixels, as shown in Figure (2d). Aggregating more frames lowers this difference as less saturation occurs. This is shown in Figure (2e). Figures (2f) to (2i) are 2-dimensional and 1-dimensional histograms of the estimated positions for points A and B in Figure (2c). These histograms show the effect of saturation on the estimated positions. The standard deviation of the estimated positions is five times higher for the frames in point A than in point B.

3.2. Empirical results

The empirical experiment was conducted at a constant rate of approximately 1000 expected photons per image, varying the ratio between frame rate and exposure time. At this photon count, the theorized uncertainty is around 6.5 nm. Figure (3f) gives the achieved uncertainty for the localized emitters. The shaded area gives the density of the localizations with the vertical bars depicting the interquartile range. The spread in the achieved uncertainty is attributed to the different blinking durations of the emitters and thus different true intensities. The Poissonian and binomial CRLB are plotted to give the theoretical uncertainty. The two CRLBs start differing from one another below 4000 frames per second. A twofold difference in uncertainty was measured for 16 aggregated frames at a frame rate of 660 frames per second.
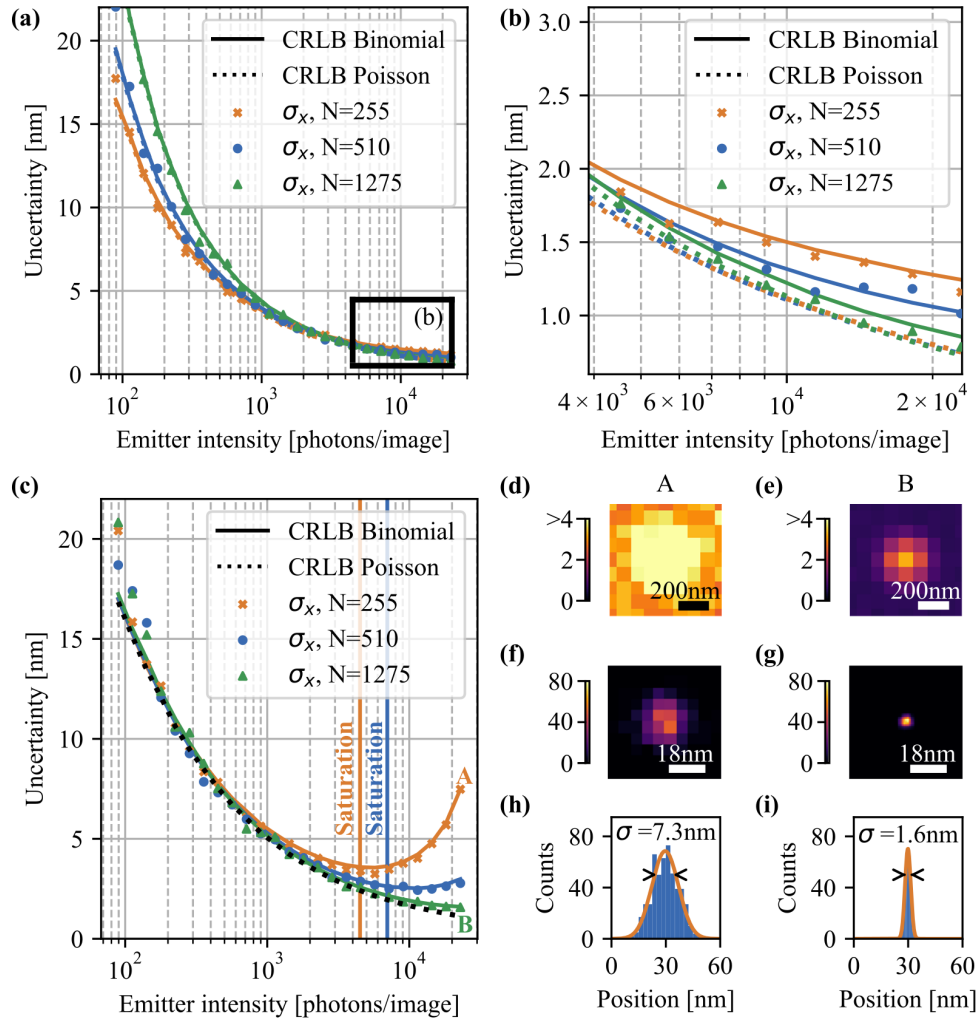
Fig. 2. Results of simulations at different intensities and aggregation. **(a)** Theorized and achieved uncertainty σ_x for simulated SPAD array images for different numbers of aggregated frames (N) and constant background of 2.5 photons per pixel. The binomial and Poissonian CRLB models are plotted, where the total exposure time is constant for each intensity. The binomial and Poissonian CRLB are identical for all lower intensities. **(b)** Zoom of the highest intensities in (a). At this point the binomial and Poissonian CRLB start deviating while the estimated uncertainties follow the binomial CRLB. **(c)** Same setting as (a), but with background noise equal to 3% of the emitter intensity, which causes the Poissonian CRLB to be identical for all aggregations. Points A and B show the effect of aggregating 255 frames versus 1275 frames. The vertical lines show the intensity where the expected photon count is larger than one for all pixels within one standard deviation of the Gaussian point spread function No saturation occurs for 1275 aggregated frames. **(d-e)** Examples of one of the 500 simulated SPAD images of 255 1275 aggregated binary frames. The scale bar gives the expected number of photons per frame. In A, the exposure time per frame is five times higher than in B, resulting in more saturation. **f-g** 2D histograms of the 500 estimated positions based on simulated SPAD images for point A and B. The histograms resemble a 2D Gaussian distribution. **(h-i)** 1D histogram of the estimated positions. The standard deviation σ_x of the fitted Gaussian distribution is used as the uncertainty in plots (a-c).
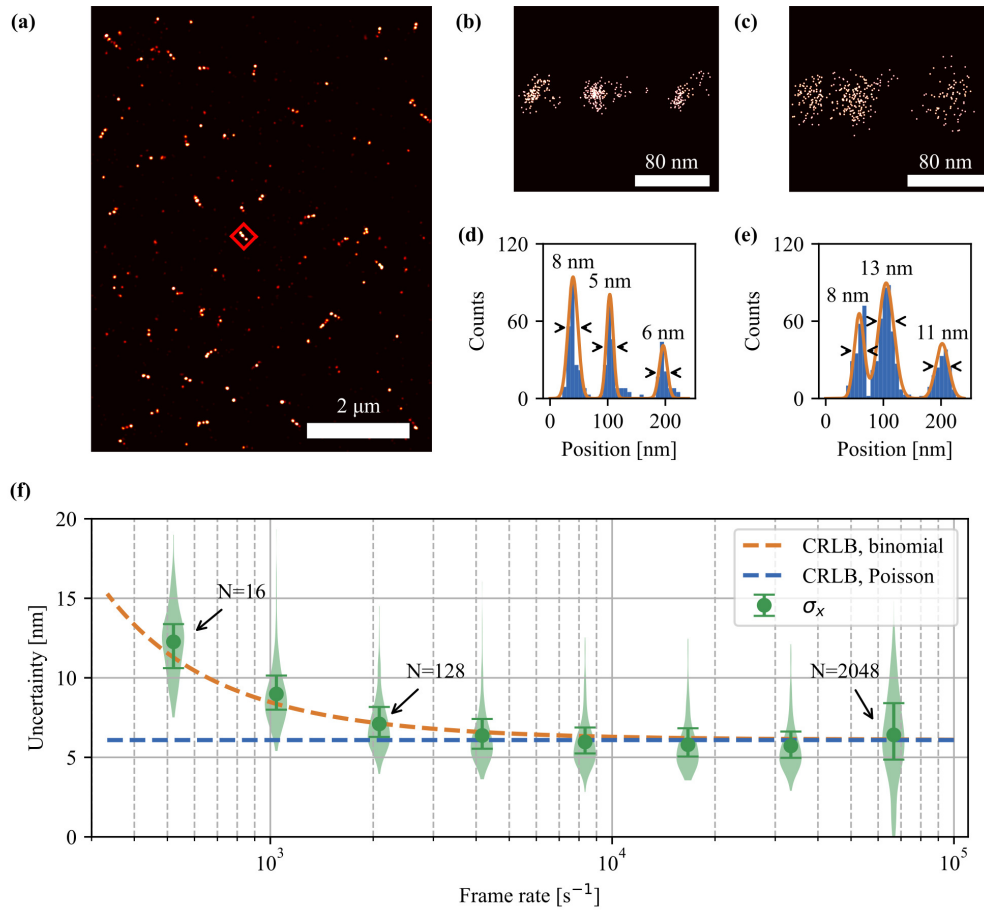
Fig. 3. Results of empirical experiment with the SwissSPAD2. **(a)** 10μm field of view of the SwissSPAD2 with 80 nm spaced nanorulers (see Supplementary Figure (S5) for the complete field of view). For this field of view an exposure time of 15 μs was used and 2048 frames were aggregated. **(b)** Zoom in of (a) on one 80 nm spaced nanoruler with approximately 370 localizations. **(c)** The same nanoruler as in (b), but with an exposure time of 1.9 ms and 16 aggregated frames. **(d)** Localization histogram of the nanoruler in (b). The standard deviation of the Gaussian fits is the uncertainty σ_x. **(e)** Localization histogram of the nanoruler in (c). The standard deviation is higher than that in (d) and the localizations of the middle binding spot are biased towards the nearby left binding spot. **(f)** The achieved mean uncertainty for different frame rates and different aggregations, but a constant total exposure time of 31 ms. The theorized minimum uncertainty was plotted using the binomial and Poissonian model. The shaded area shows the distribution of the localization uncertainty and the error bars represent the first and fourth quarter. The CRLBs overlap at high frame rates and start differing below 128 aggregated frames. The SwissSPAD achieves the Cramér-Rao lower bound for all frame rates.

4. Conclusions

SPAD arrays have a high frame rate but output binary frames. This fundamentally changes the image formation model used for SMLM applications, which assumes photon arrivals to follow a Poissonian distribution. The image formation model is used to calculate the theoretical minimum uncertainty that can be achieved in SMLM by calculating the CRLB [11]. Using the theoretical minimum uncertainty, it is possible to predict and benchmark the achieved uncertainty for a particular localization approach. Recent research into using SPAD arrays for SMLM [2, 5, 13] has not yet derived the theoretical minimum uncertainty when using a SPAD array. In this paper, we propose a binomial CRLB specifically for SMLM with a SPAD array.

We have shown that if saturation occurs, the theorized uncertainty of the binomial CRLB is 46% higher than the Poissonian CRLB. Saturation occurs if all pixels within one standard deviation of the point spread function have more than one expected photon arrival during one frame period. In simulations, individual pixels were saturated by modelling pixels up to four photon arrivals per frame period. For this case there was a factor five difference between the theorized uncertainty of the Poissonian CRLB and the proposed binomial CRLB, which was confirmed by the achieved uncertainty in the simulation.

Further investigation into this difference using empirical data demonstrated that saturation is unlikely to occur in SMLM. The difference between the Poissonian and binomial CRLB was limited to twofold for low frame rates and negligible for high frame rates, where no saturation occurred. Therefore, the binomial CRLB can be used to predict and benchmark localization uncertainty for SMLM with SPAD arrays for all practical intensities, but is especially relevant if saturation is present.

The empirical data in this research was limited by the photon detection efficiency of the SwissSPAD and nanoruler intensity. As a consequence, it was impossible to reproduce the big difference between the binomial and Poissonian theoretical uncertainty in the empirical experiment. Thus the binomial CRLB will become more important as the photon detection probability of SPAD devices increases in the future.

A further study could assess the theoretical uncertainty of SPAD arrays in super-resolution methods other than SMLM. The high frame rate of the SPAD array can prove to be a valuable contribution to single-molecule tracking for instance. This method will benefit from the binomial CRLB when what exposure time to use in the trade-off between localization uncertainty and displacement due to Brownian motion. We also see applications for the findings of this study in time-of-flight imaging. This type of imaging is susceptible to pixel saturation because of the unpredictable reflectivity of objects. It will therefore benefit from the binomial CRLB proposed in this paper by allowing researchers to benchmark their uncertainty to the theoretical minimum uncertainty.

5. Backmatter

Data Availability Statement. Data from the empirical experiment presented in this paper are available in Ref. [21].

Supplemental document. See the Supplement 1 for supporting content.

References

1. S. Burri, F. Powolny, C. E. Bruschini, X. Michalet, F. Regazzoni, and E. Charbon, "A 65k pixel, 150k frames-per-second camera with global gating and micro-lenses suitable for fluorescence lifetime imaging," in *Optical Sensing*

and Detection III, vol. 9141 F. Berghmans, A. G. Mignani, and P. D. Moor, eds., International Society for Optics and Photonics (SPIE, 2014), pp. 55 – 61.

2. I. Gyongy, A. Davies, N. A. W. Dutton, R. R. Duncan, C. Rickman, R. K. Henderson, and P. A. Dalgarno, "Smart-aggregation imaging for single molecule localisation with SPAD cameras," Sci. Reports **6**, 37349 (2016).

3. I. M. Antolovic, S. Burri, C. Bruschini, R. Hoebe, and E. Charbon, "Nonuniformity analysis of a 65-kpixel cmos SPAD imager," IEEE Transactions on Electron Devices **63**, 57–64 (2016).

4. V. Krishnaswami, C. J. F. Van Noorden, E. M. M. Manders, and R. A. Hoebe, "Towards digital photon counting cameras for single-molecule optical nanoscopy," Opt. Nanoscopy **3**, 1 (2014).

5. I. Gyongy, A. Davies, A. M. Crespo, A. Green, N. A. W. Dutton, R. R. Duncan, C. Rickman, R. K. Henderson, and P. A. Dalgarno, "High-speed particle tracking in microscopy using SPAD image sensors," in *High-Speed Biomedical Imaging and Spectroscopy III: Toward Big Data Instrumentation and Management,* vol. 10505 K. K. Tsia and K. Goda, eds., International Society for Optics and Photonics (SPIE, 2018), pp. 29 – 34.

6. A. Ulku, A. Ardelean, M. Antolovic, S. Weiss, E. Charbon, C. Bruschini, and X. Michalet, "Wide-field time-gated SPAD imager for phasor-based FLIM applications," Methods Appl. Fluoresc. **8**, 024002 (2020).

7. H. A. R. Homulle, F. Powolny, P. L. Stegehuis, J. Dijkstra, D.-U. Li, K. Homicsko, D. Rimoldi, K. Muehlethaler, J. O. Prior, R. Sinisi, E. Dubikovskaya, E. Charbon, and C. Bruschini, "Compact solid-state cmos single-photon detector array for in vivo nir fluorescence lifetime oncology measurements," Biomed. Opt. Express **7**, 1797–1814 (2016).

8. K. Morimoto, A. Ardelean, M.-L. Wu, A. C. Ulku, I. M. Antolovic, C. Bruschini, and E. Charbon, "Megapixel time-gated SPAD image sensor for 2d and 3d imaging applications," Optica **7**, 346–354 (2020).

9. F. Heide, S. Diamond, D. B. Lindell, and G. Wetzstein, "Sub-picosecond photon-efficient 3d imaging using single-photon sensors," Sci. Reports **8**, 17726 (2018).

10. F. Zappa, S. Tisa, A. Tosi, and S. Cova, "Principles and features of single-photon avalanche diode arrays," Sensors Actuators A: Phys. **140**, 103 – 112 (2007).

11. C. S. Smith, N. Joseph, B. Rieger, and K. A. Lidke, "Fast, single-molecule localization that achieves theoretically minimum uncertainty," Nat. Methods **7**, 373–375 (2010).

12. B. Rieger, R. Nieuwenhuizen, and S. Stallinga, "Image processing and analysis for single-molecule localization microscopy: Computation for nanoscale imaging," IEEE Signal Process. Mag. **32**, 49–57 (2015).

13. I. M. Antolovic, S. Burri, C. Bruschini, R. A. Hoebe, and E. Charbon, "SPAD imagers for super resolution localization microscopy enable analysis of fast fluorophore blinking," Sci. Reports **7**, 44108 (2017).

14. B. Zhang, J. Zerubia, and J.-C. Olivo-Marin, "Gaussian approximations of fluorescence microscope point-spread function models," Appl. Opt. **46**, 1819 (2007).

15. A. Panglosse, P. Martin-Gonthier, O. Marcelot, C. Virmontois, O. Saint-Pe, and P. Magnan, "Dark count rate modeling in single-photon avalanche diodes," IEEE Transactions on Circuits Syst. I: Regul. Pap. **67**, 1507–1515 (2020).

16. I. Antolovic, "SPAD imagers for super resolution microscopy," Ph.D. thesis (2018).

17. S. M. Kay, *Fundamentals of Statistical Signal Processing: Estimation Theory* (Prentice-Hall, Inc., Upper Saddle River, NJ, USA, 1993).

18. A. C. Ulku, C. Bruschini, I. M. Antolovic, Y. Kuo, R. Ankri, S. Weiss, X. Michalet, and E. Charbon, "A 512 × 512 SPAD image sensor with integrated gating for widefield FLIM," IEEE J. Sel. Top. Quantum Electron. **25**, 1–12 (2019).

19. J. Cnossen, T. Hinsdale, R. Ø. Thorsen, M. Siemons, F. Schueder, R. Jungmann, C. S. Smith, B. Rieger, and S. Stallinga, "Localization microscopy at doubled precision with patterned illumination," Nat. Methods **17**, 59–63 (2020).

20. J. Cnossen, T. J. Cui, C. Joo, and C. Smith, "Drift correction in localization microscopy using entropy minimization," bioRxiv (2021).

21. Q. Houwink, D. Kalisvaart, S.-T. Hung, J. Cnossen, D. Fan, P. Mos, A. C. Ülkü, E. Charbon, and C. Smith, "SwissSPAD2 images of nanorulers acquired using total internal reflection fluorescence microscopy," (2021). 4TU.ResearchData.

Theoretical Minimum Uncertainty of Single-Molecule Localizations Using a Single-Photon Avalanche Diode: supplemental document

S1. DERIVATION OF THE LIKELIHOOD FOR A SINGLE-PHOTON AVALANCHE DIODE ARRAY

It is assumed that the point spread function (PSF) of an emitter with coordinates $[\theta_x, \theta_y]$ has a Gaussian form as shown in Equation (S1) [1]. σ is the standard deviation of the PSF. This can be discretized over the pixels of size $[\Delta x, \Delta y]$, scaled by the emitter intensity θ_I, and supplemented by the background intensity θ_b to obtain Equation (S2). The error function, denoted as *erf*, deals with the integration over the pixels. $\mu(x_k, y_k, \theta)$ is now the expression for the expected number of photon arrivals in pixel k, given parameters $\theta = [\theta_x, \theta_y, \theta_I, \theta_b]$ and pixel position $[x_k, y_k]$, and is furthermore referred to as μ_k.

$$h(x,y)^2 = \frac{1}{2\pi\sigma^2} e^{\frac{-x^2-y^2}{2\sigma^2}} \tag{S1}$$

$$\mu\left(x_k, y_k, \theta\right) = \theta_I P\left(\theta_x, \theta_y\right) E_x\left(x_k, \theta_x\right) E_y\left(y_k, \theta_y\right) + \theta_b \Delta x \Delta y$$

$$E_x\left(x_k, \theta_x\right) = \frac{1}{2}\operatorname{erf}\left(\frac{x_k - \theta_x + \frac{\Delta x}{2}}{\sigma\sqrt{2}}\right) - \frac{1}{2}\operatorname{erf}\left(\frac{x_k - \theta_x - \frac{\Delta x}{2}}{\sigma\sqrt{2}}\right) \tag{S2}$$

$$E_y\left(y_k, \theta_y\right) = \frac{1}{2}\operatorname{erf}\left(\frac{y_k - \theta_y + \frac{\Delta y}{2}}{\sigma\sqrt{2}}\right) - \frac{1}{2}\operatorname{erf}\left(\frac{y_k - \theta_y - \frac{\Delta y}{2}}{\sigma\sqrt{2}}\right)$$

The next step is to account for the photon noise inherent to optical imaging. For continuously imaging cameras the expected photon count can be inserted into a Poisson distribution as its mean. However, a SPAD array measures a maximum of one photon, even when there are more than one incident photons during the exposure time. To account for this, the probabilities of observing a nonzero quantity of photons are summed, as shown in Equation (S3), where t_e is the exposure time of the SPAD array and c_k is the observed number of photons in pixel k.

Additionally, a SPAD array experiences a pixel-dependent noise, known as the dark count rate (DCR). The number of dark counts in a frame is not dependent on the size of the pixel and is also not subject to the PSF, it is however dependent on the exposure time t_e. The dark counts per frame are defined as $DCR \times t_e$. DCR is denoted as a vector containing all pixel dependent dark count rates, i.e. $DCR = [DCR_1, DCR_2, \ldots, DCR_n]$, where n is the number of pixels in the region of interest.

Upon aggregating N frames, the probability of observing $c_k^{(N)}$ photons in pixel k is given in Equation (S4). Here $C_k^{(N)}$ is the random variable for the number of photons after aggregating N frames. The expected photon rate $\mathbb{E}\left[C_k^{(N)}\right]$ and its variance $\operatorname{Var}(C_K^{(N)})$ when aggregating N photons follow from Equation (S4) and are given in Equation (S5).

$$P(C_k \geq 1) = 1 - P(C_k = 0) = 1 - e^{-t_e(\mu_k + DCR_k)} \tag{S3}$$

$$P(C_k^{(N)} = c_k^{(N)}) = \binom{N}{c_k^{(N)}} (1 - e^{-t_e(\mu_k - DCR_k)})^{c_k^{(N)}} e^{-t_e(\mu_k + DCR_k)(N - c_k^{(N)})} \tag{S4}$$

$$\mathbb{E}\left[C_k^{(N)}\right] = N\left(1 - e^{-t_e(\mu_k + DCR_k)}\right)$$
$$\text{var}(C_k^{(N)}) = Ne^{-t_e(\mu_k + DCR_k)}\left(1 - e^{-t_e(\mu_k + DCR_k)}\right)$$
(S5)

S2: DERIVATION OF THE CRAMÉR-RAO LOWER BOUND FOR A SINGLE-PHOTON AVALANCHE DIODE ARRAY

Using the image model of Equation (S2), probability mass function in Equation (S4) and the estimated DCR, the optimal values for the parameter vector θ can be estimated. We used maximum likelihood estimation (MLE) for this. Given a data set $c = [c_1, c_2, ..., c_n]$ of observed photon counts in all pixels, the likelihood of this data set is calculated in Equation (S6).

To prevent numerical issues, the MLE is often altered such that it maximizes the log-likelihood, yielding the same result. The log-likelihood is derived in Equation (S7). The log of the binomial coefficient is not explored further as all terms drop out in further steps.

$$L(\theta|c) = \prod_{k=1}^{n} \binom{N}{c_k^{(N)}} (1 - e^{-t_e(\mu_k + DCR_k)})^{c_k^{(N)}} e^{-t_e(\mu_k + DCR_k)(N - c_k^{(N)})}$$
(S6)

$$l(\theta|c) = \sum_{k=1}^{n} \left(\log\binom{N}{c_k^{(N)}} + c_k^{(N)}\log\left(1 - e^{-t_e(\mu_k + DCR_k)}\right) - t_e(\mu_k + DCR_k)(N - c_k) \right)$$
(S7)

Based on the log-likelihood of the SPAD image model derived in Equation (S7) the Cramér Rao Lower Bound (CRLB) can be derived. The CRLB expresses a lower bound on the variance that an unbiased estimator can achieve. The CRLB is defined as the diagonal entries of the inverse of the Fisher Matrix $I_{ij}(\theta)$, for which Equation (S8) holds.

$$I_{ij}(\theta) = -\mathbb{E}\left[\frac{\partial l(\theta|c)}{\partial \theta_i \partial \theta_j}\right] = \mathbb{E}\left[\frac{\partial l(\theta|c)}{\partial \theta_i}\frac{\partial l(\theta|c)}{\partial \theta_j}\right]$$
(S8)

Next, the partial derivative of the log-likelihood with respect to an arbitrary parameter, θ_i, is derived in Equation (S9). θ_i is a parameter of μ_k. The Fisher matrix is now easily given in Equation (S10). The terms $N(1 - e^{-\mu_l t_e - DCR_l})$ and $N(1 - e^{-t_e(\mu_k + DCR_k)})$ are equal to $\mathbb{E}\left[C_l^N\right]$ and $\mathbb{E}\left[C_k^{(N)}\right]$ respectively, as shown in Equation (S5). It follows from this that the product of the numerators in the expectation represents the covariance of $C_k^{(N)}$ and $C_l^{(N)}$, i.e. $\mathbb{E}\left[\left(C_k^{(N)} - \mathbb{E}\left[C_k^{(N)}\right]\right)\left(C_l^{(N)} - \mathbb{E}\left[C_l^{(N)}\right]\right)\right]$.

It is assumed that there is no correlation between pixels, i.e. no crosstalk [2] and therefore $C_k^{(N)}$ and $C_l^{(N)}$ are independent. It thus holds that the covariance is 0 for $k \neq l$ and is equal to the variance for $k = l$. The variance was derived in Equation (S5) and can be used to simplify Equation (S10) to get a simplified expression for the Fisher matrix.

$$\frac{\partial l(\theta|c)}{\partial \theta_i} = \sum_{k=1}^{n} \left(\left(\frac{c_k^{(N)} t_e e^{-t_e(\mu_k + DCR_k)}}{1 - e^{-t_e(\mu_k + DCR_k)}} - t_e(N - c_k^{(N)}) \right) \frac{\partial \mu_k}{\partial \theta_i} \right)$$
$$= t_e \sum_{k=1}^{n} \left(\frac{c_k^{(N)} - N(1 - e^{-t_e(\mu_k + DCR_k)})}{1 - e^{-t_e(\mu_k + DCR_k)}} \frac{\partial \mu_k}{\partial \theta_i} \right)$$
(S9)

$$I_{ij}(\theta) = \frac{1}{t_e^2} \mathbb{E} \left[\sum_{k=1}^{n} \sum_{l=1}^{n} \left(\frac{c_k^{(N)} - N(1 - e^{-t_e(\mu_k + DCR_k)})}{1 - e^{-t_e(\mu_k + DCR_k)}} \right) \left(\frac{c_l^{(N)} - N(1 - e^{-\mu_l t_e - DCR_l})}{1 - e^{-t_e(\mu_l + DCR_l)}} \right) \frac{\partial \mu_k}{\partial \theta_i} \frac{\partial \mu_l}{\partial \theta_j} \right]$$

$$= Nt_e^2 \sum_{k=1}^{n} \left(\frac{\partial \mu_k}{\partial \theta_i} \frac{\partial \mu_k}{\partial \theta_j} \frac{e^{-\mu_k t_e - DCR_i} \left(1 - e^{-t_e(\mu_k + DCR_i)} \right)}{\left(1 - e^{-t_e(\mu_k + DCR_k)} \right)^2} \right)$$

$$= Nt_e^2 \sum_{k=1}^{n} \left(\frac{\partial \mu_k}{\partial \theta_i} \frac{\partial \mu_k}{\partial \theta_j} \frac{e^{-t_e(\mu_k + DCR_i)}}{1 - e^{-t_e(\mu_k + DCR_k)}} \right)$$

(S10)

The partial derivatives of μ_k with respect to the different parameters in θ have been derived in [1] and are given in Equation (S11).

$$\frac{\partial \mu_k}{\partial \theta_x} = \frac{\theta_I}{\sqrt{2\pi}\sigma} \left(e^{\frac{-\left(x_k - \theta_x - \frac{1}{2}\right)^2}{2\sigma^2}} - e^{\frac{-\left(x_k - \theta_x + \frac{1}{2}\right)^2}{2\sigma^2}} \right) \Delta E_y(x, y) \tag{S11a}$$

$$\frac{\partial \mu_k}{\partial \theta_y} = \frac{\theta_I}{\sqrt{2\pi}\sigma} \left(e^{\frac{-\left(y_k - \theta_y - \frac{1}{2}\right)^2}{2\sigma^2}} - e^{\frac{-\left(y_k - \theta_y + \frac{1}{2}\right)^2}{2\sigma^2}} \right) \Delta E_x(x, y) \tag{S11b}$$

$$\frac{\partial \mu_k}{\partial \theta_I} = \Delta E_x(x, y) \Delta E_y(x, y) \tag{S11c}$$

$$\frac{\partial \mu_k}{\partial \theta_b} = 1 \tag{S11d}$$

To find the maximum likelihood, the Levenberg-Marquardt method is applied. Using this method the root of the derivative of the log-likelihood can be found. The parameters are updated as in Equation (S12), where a is the iteration and $\frac{\partial l(\theta|\vec{x})}{\partial \theta_i}$ and $\frac{\partial^2 l(\theta|\vec{x})}{\partial \theta_i^2}$ are given in Equations (S9) and (S13), respectively. λ operates as a relaxation constant.

$$\theta_{i,a+1} = \theta_{i,a} - \left(\frac{\partial^2 l(\theta|c)}{\partial \theta_i^2} - \lambda I_4 \right)^{-1} \frac{\partial l\theta|c)}{\partial \theta_i} \tag{S12}$$

$$\frac{\partial^2 l(\theta|c)}{\partial \theta_i \partial \theta_j} = t_e \sum_{k=1}^{n} \left[\frac{\partial^2 \mu_k}{\partial \theta_i \partial_j} \frac{c_k^{(N)} - N(1 - e^{-t_e(\mu_k + DCR_k)})}{(1 - e^{-t_e(\mu_k + DCR_k)})} + \frac{\partial \mu_k}{\partial \theta_i} \frac{\partial \mu_k}{\partial \theta_j} \right.$$

$$\left. \times \left(\frac{-Nt_e e^{-t_e(\mu_k + DCR_k)}(1 - e^{-t_e(\mu_k + DCR_k)}) - t_e e^{-t_e(\mu_k + DCR_k)} \left(c_k^{(N)} - N \left(1 - e^{-t_e(\mu_k + DCR_k)} \right) \right)}{(1 - e^{-t_e(\mu_k + DCR_k)})^2} \right) \right]$$

$$= t_e \sum_{k=1}^{n} \left[\frac{\partial^2 \mu_k}{\partial \theta_i \partial \theta_j} \frac{c_k^{(N)} - N(1 - e^{-t_e(\mu_k + DCR_k)})}{(1 - e^{-t_e(\mu_k + DCR_k)})} - \frac{\partial \mu_k}{\partial \theta_j} \frac{t_e e^{-t_e(\mu_k + DCR_k)} c_k^{(N)}}{\left(1 - e^{-t_e(\mu_k + DCR_k)} \right)} \right]$$

(S13)

The second partial derivatives of μ_k with respect to the different parameters in θ have been derived in [1] and are given in Equation (S14).

$$\frac{\partial^2 \mu_k}{\partial \theta_x^2} = \frac{\theta_I}{\sqrt{2\pi}\sigma^3} \left(\left(x_k - \theta_x - \frac{1}{2} \right) e^{\frac{-\left(x_k - \theta_x - \frac{1}{2} \right)^2}{2\sigma^2}} - \left(x_k - \theta_x + \frac{1}{2} \right) e^{\frac{-\left(x_k - \theta_x + \frac{1}{2} \right)^2}{2\sigma^2}} \right) \Delta E_y(x,y)$$

$$\text{(S14a)}$$

$$\frac{\partial^2 \mu_k}{\partial \theta_x \partial \theta_y} = \frac{\theta_I}{2\pi\sigma^2} \left(e^{\frac{-\left(x_k - \theta_x - \frac{1}{2} \right)^2}{2\sigma^2}} - e^{\frac{-\left(x_k - \theta_x + \frac{1}{2} \right)^2}{2\sigma^2}} \right) \left(e^{\frac{-\left(y_k - \theta_y - \frac{1}{2} \right)^2}{2\sigma^2}} - e^{\frac{-\left(y_k - \theta_y + \frac{1}{2} \right)^2}{2\sigma^2}} \right) \quad \text{(S14b)}$$

$$\frac{\partial^2 \mu_k}{\partial \theta_x \partial \theta_I} = \frac{1}{\sqrt{2\pi}\sigma} \left(e^{\frac{-\left(x_k - \theta_x - \frac{1}{2} \right)^2}{2\sigma^2}} - e^{\frac{-\left(x_k - \theta_x + \frac{1}{2} \right)^2}{2\sigma^2}} \right) \Delta E_y(x,y) \quad \text{(S14c)}$$

$$\frac{\partial^2 \mu_k}{\partial \theta_x \partial \theta_b} = 0 \quad \text{(S14d)}$$

$$\frac{\partial^2 \mu_k}{\partial \theta_y \partial \theta_x} = \frac{\theta_I}{2\pi\sigma^2} \left(e^{\frac{-\left(y_k - \theta_y - \frac{1}{2} \right)^2}{2\sigma^2}} - e^{\frac{-\left(y_k - \theta_y + \frac{1}{2} \right)^2}{2\sigma^2}} \right) \left(e^{\frac{-\left(x_k - \theta_x - \frac{1}{2} \right)^2}{2\sigma^2}} - e^{\frac{-\left(x_k - \theta_x + \frac{1}{2} \right)^2}{2\sigma^2}} \right) \quad \text{(S14e)}$$

$$\frac{\partial^2 \mu_k}{\partial \theta_y^2} = \frac{\theta_I}{\sqrt{2\pi}\sigma^3} \left(\left(y_k - \theta_y - \frac{1}{2} \right) e^{\frac{-\left(y_k - \theta_y - \frac{1}{2} \right)^2}{2\sigma^2}} - \left(y_k - \theta_y + \frac{1}{2} \right) e^{\frac{-\left(y_k - \theta_y + \frac{1}{2} \right)^2}{2\sigma^2}} \right) \Delta E_x(x,y)$$

$$\text{(S14f)}$$

$$\frac{\partial^2 \mu_k}{\partial \theta_y \partial \theta_I} = \frac{1}{\sqrt{2\pi}\sigma} \left(e^{\frac{-\left(y_k - \theta_y - \frac{1}{2} \right)^2}{2\sigma^2}} - e^{\frac{-\left(y_k - \theta_y + \frac{1}{2} \right)^2}{2\sigma^2}} \right) \Delta E_x(x,y) \quad \text{(S14g)}$$

$$\frac{\partial^2 \mu_k}{\partial \theta_y \partial \theta_b} = 0 \quad \text{(S14h)}$$

$$\frac{\partial^2 \mu_k}{\partial \theta_I \partial \theta_x} = \frac{1}{2\pi\sigma^2} \left(e^{\frac{-\left(x_k - \theta_x - \frac{1}{2} \right)^2}{2\sigma^2}} - e^{\frac{-\left(x_k - \theta_x + \frac{1}{2} \right)^2}{2\sigma^2}} \right) \Delta E_y(x,y) \quad \text{(S14i)}$$

$$\frac{\partial^2 \mu_k}{\partial \theta_I \partial \theta_y} = \frac{1}{2\pi\sigma^2} \left(e^{\frac{-\left(y_k - \theta_y - \frac{1}{2} \right)^2}{2\sigma^2}} - e^{\frac{-\left(y_k - \theta_y + \frac{1}{2} \right)^2}{2\sigma^2}} \right) \Delta E_x(x,y) \quad \text{(S14j)}$$

$$\frac{\partial^2 \mu_k}{\partial \theta_I^2} = \frac{\partial^2 \mu_k}{\partial \theta_I \partial \theta_b} = 0 \quad \text{(S14k)}$$

$$\frac{\partial^2 \mu_k}{\partial \theta_b \partial \theta_x} = \frac{\partial^2 \mu_k}{\partial \theta_b \partial \theta_y} = \frac{\partial^2 \mu_k}{\partial \theta_b \partial \theta_I} = \frac{\partial^2 \mu_k}{\partial \theta_b^2} = 0 \quad \text{(S14l)}$$

S3. χ^2 FILTER

The χ^2-test can be used to verify whether a model is appropriately formulated. Additionally, it can help detect local minimums, should the optimization algorithm get stuck in one. Equation (S15) gives the expression for the χ^2 value, where p_k is the probability of detecting a photon in pixel k as given in Equation (S3).

$$\chi^2 = \sum_{k=1}^{n} \frac{(c_k^{(N)} - Np_k)^2}{Np_k} \tag{S15}$$

The threshold to accept the theoretical is commonly set at the expected value plus a pre-determined amount of standard deviations of the χ^2 value. A threshold of the expected value plus two standard deviations gives approximately a 95% level of confidence. The expected value and standard deviation of the χ^2 value are derived below. The expected values for the higher orders of $(c_k^{(N)} - \mathbb{E}[c_k^{(N)}])$ are the central moments of the binomial distribution [3]. The two relevant central moments are given as $\mathbb{E}[(c_k^{(N)} - \mathbb{E}[c_k^{(N)}])^2] = Np_k(1 - p_k)$ and $\mathbb{E}[(c_k^{(N)} - \mathbb{E}[c_k^{(N)}])^2] = Np_k(1 - p_k)(3p_k^3(2 - N) + 3p_k^2(N - 2) + 1)$.

$$
\begin{aligned}
\mathbb{E}\left[\chi^2\right] &= \sum_{k=1}^{n} \mathbb{E}\left[\frac{(c_k^{(N)} - Np_k)^2}{Np_k}\right] \\
&= \sum_{k=1}^{n} \frac{1}{Np_k}\left(\mathbb{E}\left[(c_k^{(N)})^2\right] - 2Np_k\mathbb{E}\left[c_k^{(N)}\right] + (Np_k)^2\right) \\
&= \sum_{k=1}^{n} 1 - p_k
\end{aligned}
\tag{S16}
$$

$$
\begin{aligned}
\sigma^2[\chi^2] &= \mathbb{E}\left[\left(\sum_{k}^{n} \frac{(c_{(N)} - \mathbb{E}[c_k])^2}{\mathbb{E}[c_k]} - \mathbb{E}\left[\sum_{k}^{n} \frac{(c_k - \mathbb{E}[c_k])^2}{\mathbb{E}[c_k]}\right]\right)^2\right] \\
&= \sum_{k}^{n} \mathbb{E}\left[\left(\frac{(c_k - \mathbb{E}[c_k])^2}{\mathbb{E}[c_k]} - \frac{\mathbb{E}\left[(c_k - \mathbb{E}[c_k])^2\right]}{\mathbb{E}[c_k]}\right)^2\right] \\
&= \sum_{k}^{n} \left[\frac{\mathbb{E}\left[(c_k - \mathbb{E}[c_k])^4\right]}{\mathbb{E}[c_k]^2} - \frac{\mathbb{E}\left[(c_k - \mathbb{E}[c_k])^2\right]^2}{\mathbb{E}[c_k]^2}\right] \\
&= \sum_{k=1}^{n} \frac{(1 - p_k)(2Np_k - 6p_k - 2Np_k^2 + 6p^2 + 1)}{Np_k}
\end{aligned}
\tag{S17}
$$
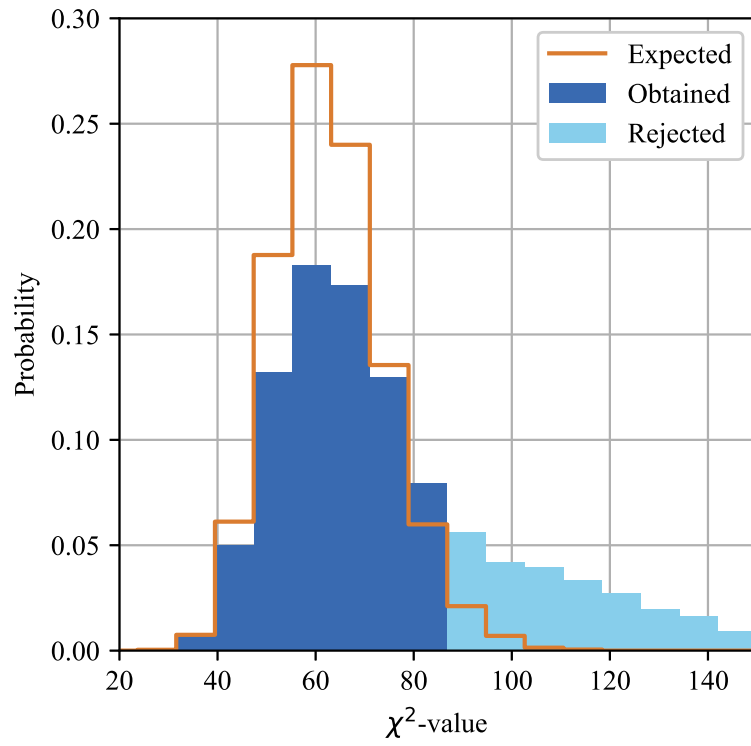
Fig. S1. χ^2-values for estimated positions and the calculated distribution. χ^2 values beyond two standard deviations from the mean are rejected.
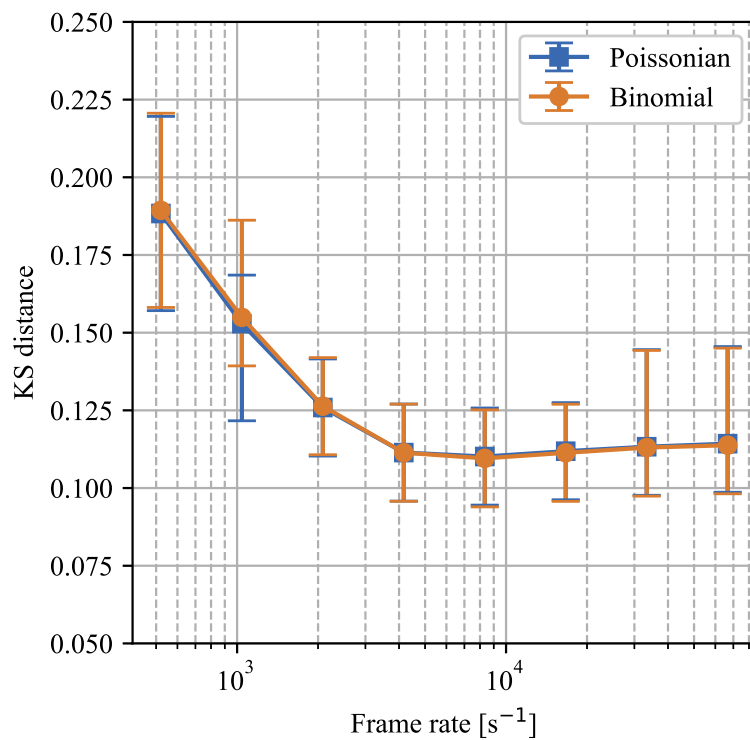
Fig. S2. Kolmogorov-Smirnov (KS) distance of the estimates with respect to a Poissonian or binomial distribution of the photon counts in an image. All estimates have a total exposure time of 31 ms, but vary in the frame rate. The vertical bars represent the interquartile range for all data points. The p-values of the KS test are not provided as the KS test does not provide a valid type 1 error rate when comparing data to a discrete distribution. Instead, the KS statistic is provided to compare the data to the two different, discrete, distributions. Similar to the Cramér-Rao lower bound, the binomial model is an equally good, or slightly better, model for all data points. The downward trend can be attributed to the stochastic effect of aggregating a small number of frames.
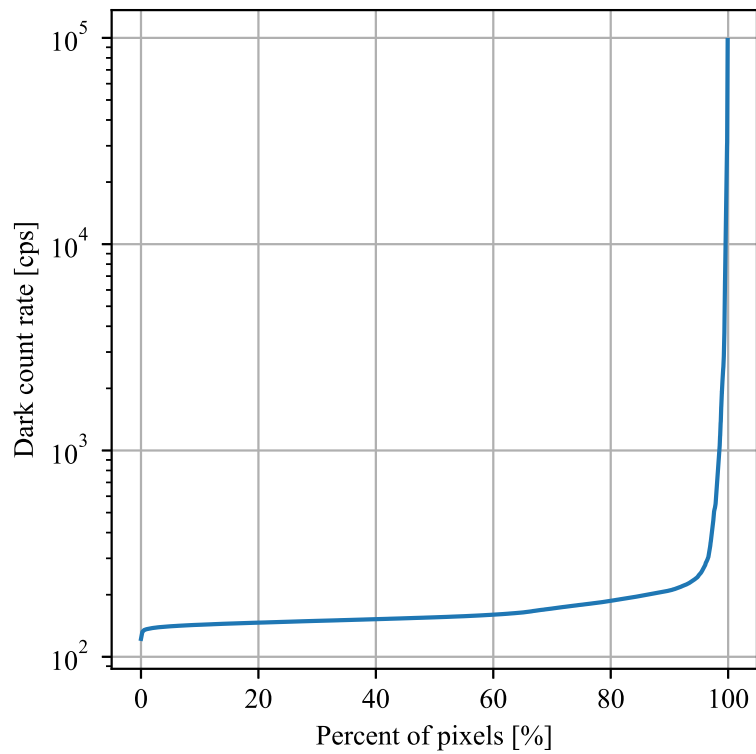
Fig. S3. Non-homogeneous dark count rate for the pixels of the SwissSPAD2. Most pixels experience limited dark count rate, while a small fraction experiences a lot of dark count rate. These pixels are known as noisy pixels and show up as bright spots in the SPAD array output.
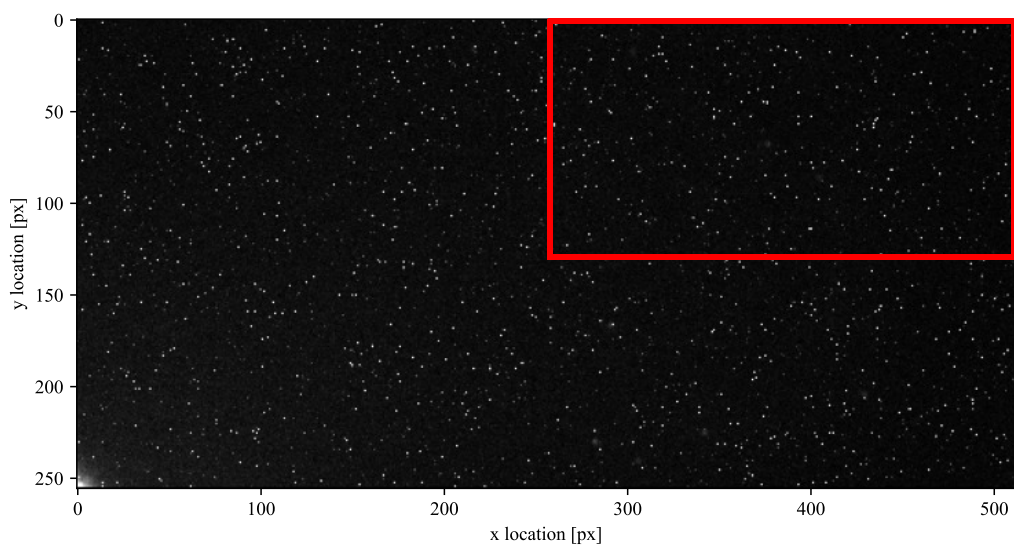
Fig. S4. Dark image acquired with the cap on. The dark count rate in each pixel is used in the image formation model. The bright corner in the bottom right is caused by leakage. Therefore, only the top right is used for the single-molecule localization.
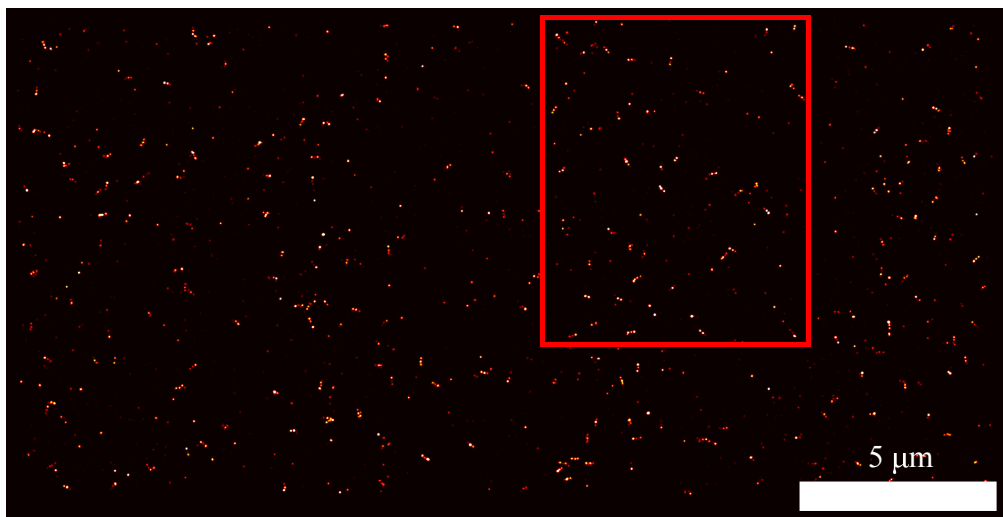
Fig. S5. Full 26 μm wide field of view of the SMLM localizations with the SPAD array using an exposure time of 15 μs and 2048 aggregated frames. The red rectangle is the field of view presented in Figure (3a) of the paper.
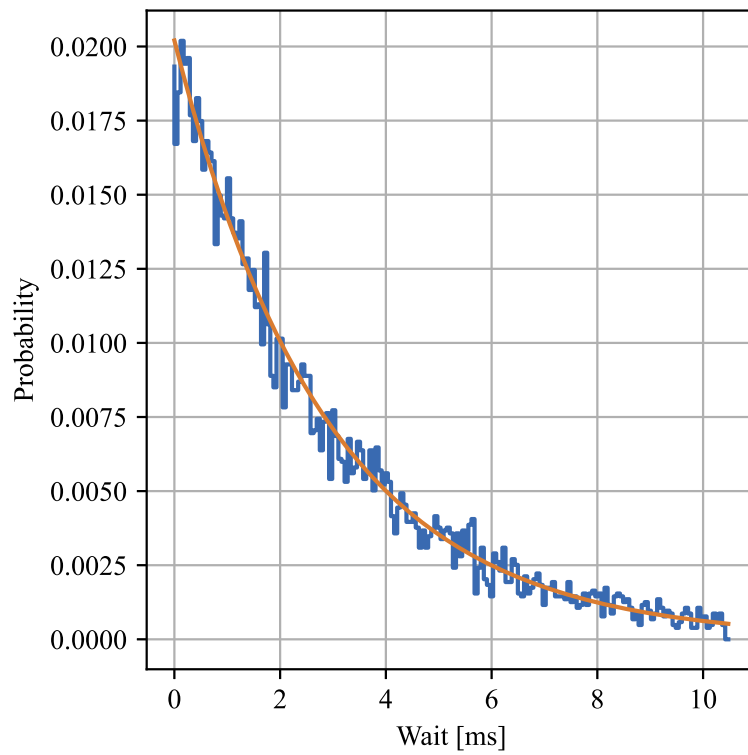
Fig. S6. Measured and expected time delays between two consecutive photon counts. A strong deviation between the measured and expected time delays would suggest afterpulsing is significant for the SwissSPAD2. This is not the case and therefore afterpulsing is neglected in the image formation model.
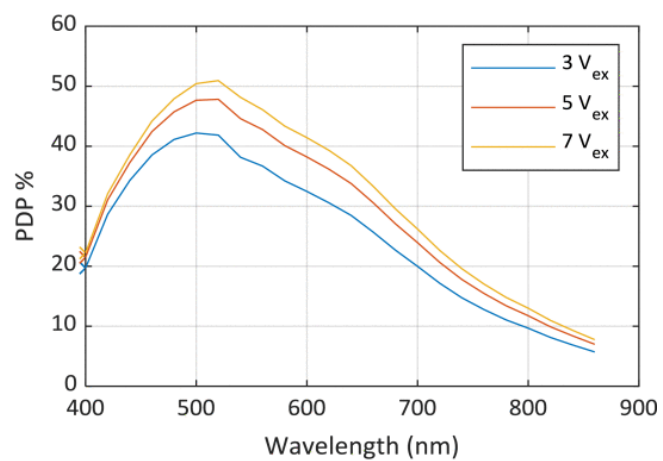
Fig. S7. Photon detection probability (PDP) of the SwissSPAD2 for different wavelengths. Fluorescent molecules that emit photons at a wavelength of 562nm, such as ATTO 542, give a higher intensity than those with a higher emission wavelength. Source: [4]

REFERENCES

1. C. S. Smith, N. Joseph, B. Rieger, and K. A. Lidke, "Fast, single-molecule localization that achieves theoretically minimum uncertainty," Nat. Methods **7**, 373–375 (2010).
2. I. Antolovic, "SPAD imagers for super resolution microscopy," Ph.D. thesis (2018).
3. A. Papoulis, *Probability, random variables, and stochastic processes* (McGraw-Hill, Boston, 2002).
4. A. C. Ulku, C. Bruschini, I. M. Antolovic, Y. Kuo, R. Ankri, S. Weiss, X. Michalet, and E. Charbon, "A 512 × 512 SPAD image sensor with integrated gating for widefield FLIM," IEEE J. Sel. Top. Quantum Electron. **25**, 1–12 (2019).

Chapter 4

Conclusion

This chapter summarizes and concludes on the findings of this thesis. Section 4-1 briefly covers the main topics of this thesis. Section 4-2 deals with points of debate in this thesis and elaborates on their effect on the results. Section 4-3 proposes further research in the field of using SPAD arrays for super-resolution microscopy. This section also touches upon an application of the binomial CRLB outside of super-resolution microscopy.

4-1 Summary

Microscopes help us to discover phenomena at a scale that is invisible to the naked eye. Unfortunately, microscopes are fundamentally limited due to the diffraction of light when passing through lenses. The diffraction limit for microscopes is calculated as $\Delta l = \frac{\lambda}{2\text{NA}}$. Here, Δl is the spatial resolution of the microscope and λ is the light wavelength. NA is the numerical aperture, defined as $NA = n_i \cdot \sin(\theta_{half})$, where n_i is the refractive index of the immersion medium and θ_{half} is the half angle of the microscope [4]. In practice, microscopes are unable to distinguish objects less than 150 nm removed from one another.

Fluorescent microscopy offers possibilities to go beyond the diffraction limit. For this type of microscopy, fluorescent molecules are excited by a laser of a particular wavelength. In response, the fluorescent molecules emit light of a different wavelength. The excitation light can be filtered such that only the emitted light is observed by an imaging device [6]. Single-molecule localization microscopy (SMLM) uses fluorescence to break the diffraction limit by sparsely exciting molecules and estimating their positions. This estimation can achieve a resolution of several nanometers [18]. DNA Point Accumulation for Imaging in Nanoscale Topography (DNA-PAINT) is a method to sparsely activate fluorescent molecules [20]. In DNA-PAINT, two types of DNA oligomers are present in the sample. One type is fixed in location and is called the docking strand. Another type, called the imaging strand, floats freely in the solvent and is connected to a fluorescent dye. At arbitrary moments, imaging strands connect to one of the docking strands. Since the docking strands are in the focal plane of the excitation light, the fluorescent dyes become visible when the imaging strand is

connected to the docking strand. After a period of time the imaging strand releases again, creating the sparse activation [15].

The emitted light is collected using an image sensor. Two types are commonly used in super-resolution microscopy. The electron multiplying charge-coupled devices (EMCCD) and the scientific complementary metal-oxide semiconductor (sCMOS) cameras [24]. Recently, a third imaging device was added to this: the single-photon avalanche diode (SPAD) array. The SPAD array is capable of imaging at 130kfps and has negligible readout noise. This makes the SPAD array an attractive option for super-resolution applications [32]. SPAD arrays experience a different type of noise, called dark count rate (DCR). DCR occurs when pixels spontaneously record a current that is not caused by a photon. Pixels suffer DCR in various degrees. Most pixels, about 99%, only experience DCR in less than 1% of the frames, while a few pixels always record a current, even in a completely dark environment. Due to its design, the SPAD array can only record one photon per pixel per exposure time. Any other photons within one exposure time are not recorded. The output of the SPAD array is therefore binary [30].

After data acquisition, SMLM applies a mathematical image process to achieve super-resolution images [17]. Using maximum likelihood estimation (MLE), an estimate is acquired of an emitter within a region of interest. To use MLE, an image formation model is required. For this image formation model, the fluorescent molecules are modelled as Gaussian point spread functions and photon arrivals are modelled as a Poissonian process. Using the image formation model, the MLE estimates the position and intensity of a molecule, as well as the background noise. After the estimation, some localizations are rejected because they do not represent a molecule but dust on the sample or noisy pixels. This rejection is performed using a χ^2-test. The standard deviation in the estimated positions for one molecule represents the uncertainty of SMLM. This uncertainty can be benchmarked to a theoretical minimum uncertainty, calculated by the Cramér-Rao lower bound (CRLB) [42]. The CRLB is a function of the emitter parameters and is derived from the likelihood.

SPAD arrays have a different image formation model than other imagers due to its binary output. Therefore, the photon count for several aggregated frames is best modelled using a binomial distribution. The success probability of the binomial distribution is equal to the sum of the probabilities of measuring more than zero photons in a Poissonian process. We have derived an image formation model using this binomial process and propose a binomial CRLB to benchmark the theoretical minimum uncertainty of the SPAD array molecule localizations.

We compared the binomial CRLB to simulated and empirical data. In simulations, a fluorescent molecule was modelled as a Gaussian point spread function. The binary SPAD array behavior was simulated by first applying a Poisson distribution to the intensity values of all pixels and then setting all values above one to one. Subsequently, multiple binary frames were aggregated. The SMLM image processing was then applied to the resulting images. The uncertainty of the resulting location estimates was compared to the Poissonian CRLB and the binomial CRLB. We found that the binomial CRLB correctly bounds the theoretical minimum uncertainty for all intensities. In contrast, the Poissonian CRLB is found to deviate 46% from the theoretical minimum uncertainty if saturation occurs. Where saturation is defined as all pixels within one standard deviation of the point spread function expecting more than one photon per frame. In simulations, the maximum difference between both CRLB models was fivefold for higher levels of saturation.

The empirical data was acquired using a TIRF microscope and DNA-PAINT. It is difficult to alter the intensity of the fluorescent molecules in an experimental setting. Therefore, the exposure time per frame and number of aggregated frames were altered such that each point has the same total exposure time, but more or less likeliness to contain saturated pixels. Each image had an expected photon count of approximately 1000. It was found that the binomial CRLB follows the achieved uncertainty for all numbers of aggregated frames. The Poissonian CRLB is nearly identical, except for long exposure times, where saturation occurs. In the experimental data, there was a twofold maximum difference between the Poissonian and binomial CRLB.

We conclude that the binomial CRLB should be used if the SPAD array frames saturate. At lower intensities, which is usually the case in SMLM, the binomial and Poissonian CRLB are identical in their performance.

4-2 Discussion

There are a few discussion points in the simulations and empirical experiments described in this thesis. In this section the most important points are mentioned and their effects on the results are covered.

Validating the binomial CRLB through simulations allows for testing in a controlled environment. Unfortunately, this controlled environment does not always give realistic results. The simulated intensity of the fluorescent molecule was increased to four expected photons for some pixels per frame. This gave a lot of saturation and led to a big difference between the binomial CRLB and the Poissonian CRLB. In empirical data it was observed that four expected photons per pixel per frame is extremely unlikely to happen. We still decided to include these high intensities to visualize the region where the two CRLBs differ by a factor five.

The empirical data give a more realistic overview of the uncertainties that one could expect when conducting SMLM. When using the SPAD array at maximum frame rate and aggregating large numbers of frames the Poissonian and binomial CRLB are nearly identical. One thing that was neglected in the empirical data is the blinking of fluorescent molecules. This blinking behavior causes the molecules to emit photons in some of the frames within an aggregated image, but not always all. As a consequence, the intensity of a molecule can be underestimated when blinking is taken into account. This means that the calculated CRLB gives a lower uncertainty than is achievable for a molecule. As a consequence, the achieved uncertainties in the empirical results of Chapter 3 do not correspond exactly with the reported CRLB.

The dark count rate measured with the SwissSPAD2 was much higher than recorded in previous research. Our research measured a median DCR of 150 cps versus a previously measured median DCR of 7.5 cps [38]. This higher DCR is likely caused by high temperatures in the detection chip and could be lowered by better cooling equipment. Future research could lower the spread in the calculated uncertainties and increase the number of localizations by lowering the DCR.

4-3   Future outlook

The results of this thesis pave the way for future research using SPAD arrays. Here, we provide suggestions for research both within and outside the field of super-resolution microscopy.

The high frame rate of SPAD arrays could be a valuable addition to single-molecule tracking applications. In [31], it was demonstrated that the freedom offered by a SPAD array in the frame aggregation during post-processing can be applied to improve tracking precision. This holds for individual molecules, where smart-aggregation can be applied to optimize for the blinking behavior [29]. The frame aggregation can also be modified between different molecules, to optimize for their individual blinking behavior. Using the results in this thesis, it can be proven that a tracking algorithm has an optimal frame duration, even when some saturation occurs in high-flux processes. This optimal frame duration for single-molecule tracking is a trade-off between the root mean square displacement caused by (Brownian) motion and the localization uncertainty, where the latter can be theoretically bounded by the binomial CRLB. As was discussed in Section 4-2, the effect of smart-aggregation on the CRLB would still need to be explored further.

Outside of super-resolution microscopy, SPAD arrays are used for time-of-flight (ToF) imaging. In ToF imaging, the distance to an object is estimated by recording the time between the light leaving the laser and the light being measured by the SPAD array. This is illustrated in Figure 4-1a. SPAD arrays are suitable for this due to their picosecond photon timing precision. MLE is used to estimate the molecule position and intensity in SMLM. In ToF imaging, MLE is used to estimate the arrival time and object reflectivity. However, the binary response of SPAD arrays causes uncertainty in the arrival time for high intensity scenes [28]. This is because the SPAD array is unable to record photon arrivals after the first photon arrival. In Figure 4-1d this effect is illustrated. This problem can be solved when considering the binary behavior during time-of-flight estimation. The binary behavior is taken into account by applying a logarithmic correction to the expected photon count at a given time instance [28]. This is similar to what we did in Section 1-4-2. Our binomial CRLB could predict and benchmark the uncertainty of the distance measurements.
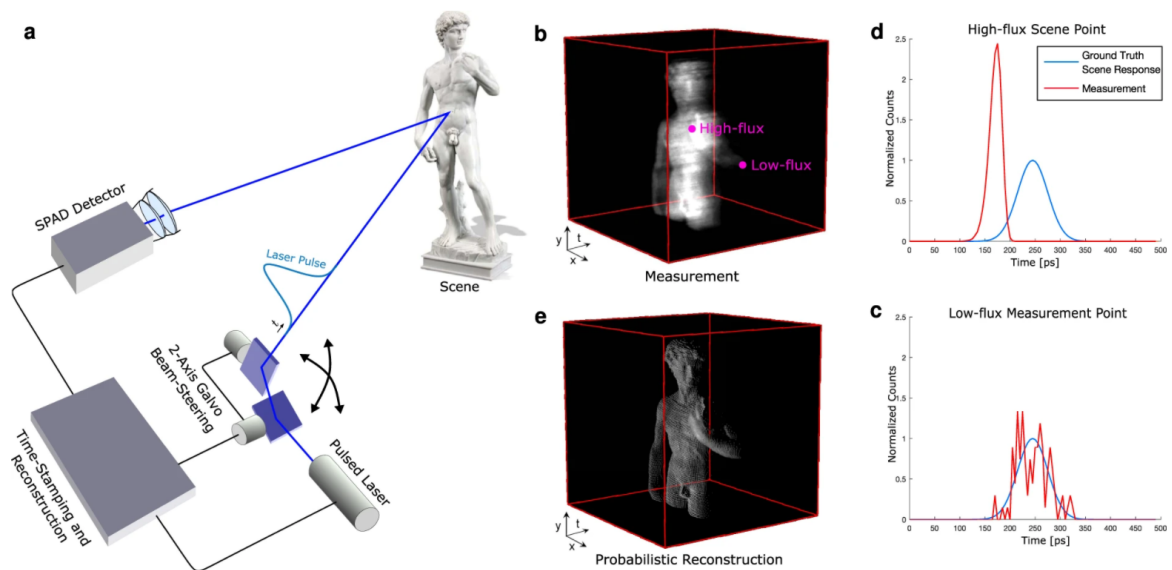
Figure 4-1: An illustration of the problem of using a SPAD array for time-of-flight (ToF) imaging. **(a)** The setup used for ToF imaging. A laser sends a Gaussian shaped pulse of light to an object. A SPAD array detects the photons reflected by the object. The time difference between the laser sending the pulse and the SPAD array detecting the pulse can be converted into a distance. **(b)** Some areas on an object of interest have higher reflectivity than others, causing high-flux and low-flow regions. **(c)** For low-flux regions, the detected photons from the sent pulses follow a Gaussian probability distribution. **(d)** For high-flux regions, the SPAD array does not detect any photons after the first photon arrival. This causes a bias of the measurement. **(e)** Upon taking this effect into account, an accurate prediction of the 3D shape of an object is reconstructed. Source: [28]

Appendix A

Image Formation Model

The image formation model describes the expected photon rate $\mu(x_k, y_k, \theta)$ in a particular pixel k, hereafter referred to as μ_k. Here, we give the mathematical derivation of μ_k as a function of the imaged object and the microscope system.

The object function $f(x, y)$, describes the shape of the object in the sample. $f(x, y, \theta)$ is given in Equation A-1, $\delta(x - \theta_x, y - \theta_y)$ is the Dirac delta function as in SMLM the molecule is assumed to be a single point in 2-dimensional space. To get a model $g(x, y)$ for the image as observed by the imaging device, the object function is convoluted with the PSF $h(x, y)^2$ [42]. As shown in Equation A-2, where the last step is possible because the first integral over the Dirac Delta function is equal to zero when $\tau \neq x - \theta_x$ or $\gamma \neq y - \theta_y$.

$$f(x, y) = \theta_I \delta(x - \theta_x, y - \theta_y) + \theta_b \tag{A-1}$$

$$
\begin{aligned}
g(x, y) =& h(x, y)^2 \circledast f(x, y) \\
g(x, y) =& h(x, y)^2 \circledast \theta_I \delta(x - \theta_x, y - \theta_y) + \theta_b \\
g(x, y) =& \iint_{\mathbb{R}^2} h(\tau, \gamma)^2 \theta_I \delta(x - \tau - \theta_x, y - \gamma - \theta_y) d\tau d\gamma + \theta_b \\
g(x, y) =& \theta_I \iint_{\mathbb{R}^2} h(\tau, \gamma)^2 \delta(x - \tau - \theta_x, y - \gamma - \theta_y) d\tau d\gamma + \theta_b \\
g(x, y) =& \theta_I h(x - \theta_x, y - \theta_y)^2 + \theta_b
\end{aligned}
\tag{A-2}
$$

To account for the pixels of the imager, the function $g(x, y)$ needs to be discretized. It is assumed that pixel k has size Δx by Δy and center coordinates $\{x_k, y_k\}$. Now, $g(x, y)$ is integrated over each pixel to get the expected amount of photons μ_k in pixel k, as shown in Equation (A-3). The background noise θ_b is already defined per pixel as it is a constant and is therefore left unchanged.

$$\mu_k(x_k, y_k) = \theta_I \int_{y_k - \frac{\Delta y}{2}}^{y_k + \frac{\Delta y}{2}} \int_{x_k - \frac{\Delta x}{2}}^{x_k + \frac{\Delta x}{2}} h(x - \theta_x, y - \theta_y)^2 dx dy + \theta_b \tag{A-3}$$

It is now assumed that the PSF $h(x, y)^2$ has a Gaussian form as shown in Equation (A-4) [42]. σ is the standard deviation of the Gaussian PSF. Substituting Equation (A-4) into (A-3) yields Equation (A-5). The latter expression is split up into an x and a y component given in Equation (A-6). The error function, denoted as erf(x), deals with the remaining integrals.

$$h(x, y)^2 = \frac{1}{2\pi\sigma^2} e^{\frac{-x^2 - y^2}{2\sigma^2}} \tag{A-4}$$

$$\mu_k = \theta_I \int_{y_k - \frac{\Delta y}{2}}^{y_k + \frac{\Delta y}{2}} \int_{x_k - \frac{\Delta x}{2}}^{x_k + \frac{\Delta x}{2}} \frac{1}{2\pi\sigma^2} e^{\frac{-x^2 - y^2}{2\sigma^2}} dx dy + \theta_b$$

$$\mu_k = \theta_I \underbrace{\left(\int_{x_k - \frac{\Delta x}{2}}^{x_k + \frac{\Delta x}{2}} \frac{1}{\sigma\sqrt{2\pi}} e^{-\frac{(x-\theta_x)^2}{2\sigma^2}} \, \mathrm{d}x \right)}_{E_x(x_k, \theta_x)} \underbrace{\left(\int_{y_k - \frac{\Delta y}{2}}^{y_k + \frac{\Delta y}{2}} \frac{1}{\sigma\sqrt{2\pi}} e^{-\frac{(y-\theta_y)^2}{2\sigma^2}} \, \mathrm{d}y \right)}_{E_y(y_k, \theta_y)} + \theta_b \tag{A-5}$$

$$\mu_k = \theta_I E_x(x_k, \theta_x) E_y(y_k, \theta_y) + \theta_b$$

$$E_x(x_k, \theta_x) = \frac{1}{2} \mathrm{erf}\left(\frac{x_k - \theta_x + \frac{\Delta x}{2}}{\sigma\sqrt{2}} \right) - \frac{1}{2} \mathrm{erf}\left(\frac{x_k - \theta_x - \frac{\Delta x}{2}}{\sigma\sqrt{2}} \right)$$

$$E_y(y_k, \theta_y) = \frac{1}{2} \mathrm{erf}\left(\frac{y_k - \theta_y + \frac{\Delta y}{2}}{\sigma\sqrt{2}} \right) - \frac{1}{2} \mathrm{erf}\left(\frac{y_k - \theta_y - \frac{\Delta y}{2}}{\sigma\sqrt{2}} \right) \tag{A-6}$$

Equation A-7 gives the partial derivatives of μ_k. $\Delta E_x(x_k, \theta_x)$ and $\Delta E_y(y_k, \theta_y)$ are given in Equation A-6.

$$\frac{\partial \mu_k}{\partial \theta_x} = \frac{\theta_I}{\sqrt{2\pi}\sigma} \left(e^{\frac{-\left(x_k - \theta_x - \frac{1}{2}\right)^2}{2\sigma^2}} - e^{\frac{-\left(x_k - \theta_x + \frac{1}{2}\right)^2}{2\sigma^2}} \right) \Delta E_y(y_k, \theta_y)$$

$$\frac{\partial \mu_k}{\partial \theta_y} = \frac{\theta_I}{\sqrt{2\pi}\sigma} \left(e^{\frac{-\left(y_k - \theta_y - \frac{1}{2}\right)^2}{2\sigma^2}} - e^{\frac{-\left(y_k - \theta_y + \frac{1}{2}\right)^2}{2\sigma^2}} \right) \Delta E_x(x_k, \theta_x) \tag{A-7}$$

$$\frac{\partial \mu_k}{\partial \theta_I} = \Delta E_x(x_k, \theta_x) \Delta E_y(y_k, \theta_y)$$

$$\frac{\partial \mu_k}{\partial \theta_{bg}} = 1$$

Appendix B

χ^2 statistic

The expected value and standard deviation of the χ^2-value are derived in Equations B-1 and B-2. In these equations, the second and fourth central moments for the Poisson distribution are used to calculate the distribution of the random variable c_k around its mean [48]. These moments are given as $\mathbb{E}[(c_k - \mathbb{E}[c_k])^2] = \mathbb{E}[c_k]$ and $\mathbb{E}[(c_k - \mathbb{E}[c_k])^4] = \mathbb{E}[c_k](1 + 3\mathbb{E}[c_k])$.

$$\mathbb{E}[\chi^2] = \mathbb{E}\left[\sum_k^n \frac{(c_k - \mathbb{E}[c_k])^2}{\mathbb{E}[c_k]}\right] = \sum_k^n \frac{1}{\mathbb{E}[c_k]}\left(\mathbb{E}\left[(c_k - \mathbb{E}[c_k])^2\right]\right) = n \tag{B-1}$$

$$
\begin{aligned}
\sigma^2[\chi^2] =& \mathbb{E}\left[\left(\sum_k^n \frac{(c_k - \mathbb{E}[c_k])^2}{\mathbb{E}[c_k]} - \mathbb{E}\left[\sum_k^n \frac{(c_k - \mathbb{E}[c_k])^2}{\mathbb{E}[c_k]}\right]\right)^2\right] \\
=& \sum_k^n \mathbb{E}\left[\left(\frac{(c_k - \mathbb{E}[c_k])^2}{\mathbb{E}[c_k]} - \frac{\mathbb{E}\left[(c_k - \mathbb{E}[c_k])^2\right]}{\mathbb{E}[c_k]}\right)^2\right] \\
=& \sum_k^n \mathbb{E}\left[\left(\frac{(c_k - \mathbb{E}[c_k])^2}{\mathbb{E}[c_k]} - 1\right)^2\right] = \sum_k^n \left[\frac{\mathbb{E}\left[(c_k - \mathbb{E}[c_k])^4\right]}{\mathbb{E}[c_k]^2} - 2\frac{\mathbb{E}\left[(c_k - \mathbb{E}[c_k])^2\right]}{\mathbb{E}[c_k]} + 1\right] \\
=& \sum_k^n \left[\frac{\mathbb{E}[c_k](1 + 3\mathbb{E}[c_k])}{\mathbb{E}[c_k]^2} - 2\frac{\mathbb{E}[c_k]}{\mathbb{E}[c_k]} + 1\right] \\
=& \sum_k^n \frac{1}{\mathbb{E}[c_k]} + 2n = \sum_k^n \frac{1}{\mu_k(x_k, y_k)t_e} + 2n
\end{aligned}
$$

$$\tag{B-2}$$

Bibliography

[1] L. Robertson, J. Backer, C. Biemans, J. van Doorn, K. Krab, W. Reijnders, H. Smit, and P. Willemsen, "4 van leeuwenhoek's microscopes," in *Antoni van Leeuwenhoek*, pp. 46–70, BRILL, Jan. 2016.

[2] S. W. Hell, "Microscopy and its focal switch," *Nature Methods*, vol. 6, pp. 24–32, Jan 2009.

[3] J. Goodman, *Introduction to Fourier optics*. Englewood, Colo: Roberts & Co, 2005.

[4] E. Abbe, "Beiträge zur theorie des mikroskops und der mikroskopischen wahrnehmung," *Archiv für Mikroskopische Anatomie*, vol. 9, pp. 413–468, Dec 1873.

[5] J. Cargille, "Immersion oil and the microscope," *New York Microscopical Society Yearbook*, vol. 1, pp. 1–6, Jan 1964.

[6] I. C. Ghiran, "Introduction to fluorescence microscopy," 2011.

[7] U. Birk, *Super-resolution microscopy : a practical guide*, pp. 5–7. Mainz: Wiley-VCH, 2017.

[8] D. Auerbach, *Photophysikalische Charakterisierung von Fluoreszenzmarkern insbesondere von Fluoreszenzproteinen*. PhD thesis, 2015.

[9] J. Vogelsang, C. Steinhauer, C. Forthmann, I. H. Stein, B. Person-Skegro, T. Cordes, and P. Tinnefeld, "Make them blink: probes for super-resolution microscopy," *Chemphyschem*, vol. 11, pp. 2475–2490, Aug 2010.

[10] Y. Lin, J. J. Long, F. Huang, W. C. Duim, S. Kirschbaum, Y. Zhang, ..., and J. Bewersdorf, "Quantifying and optimizing single-molecule switching nanoscopy at high speeds," *PLOS ONE*, vol. 10, pp. 1–20, 05 2015.

[11] U. Kubitscheck, *Fluorescence Microscopy : from principles to biological applications*. Weinheim: Wiley, 2013.

[12] N. Boens, W. Qin, N. Basarić, J. Hofkens, ..., and A. Miura, "Fluorescence lifetime standards for time and frequency domain fluorescence spectroscopy," *Analytical Chemistry*, vol. 79, pp. 2137–2149, Mar 2007.

[13] D. Axelrod, *Total Internal Reflection Fluorescence Microscopy for Single-Molecule Studies*, pp. 2623–2631. Berlin, Heidelberg: Springer Berlin Heidelberg, 2013.

[14] D. Axelrod, "Chapter 7 total internal reflection fluorescence microscopy," in *Biophysical Tools for Biologists, Volume Two: In Vivo Techniques*, vol. 89 of *Methods in Cell Biology*, pp. 169 – 221, Academic Press, 2008.

[15] N. L. Thompson and B. C. Lagerholm, "Total internal reflection fluorescence: applications in cellular biophysics," *Current Opinion in Biotechnology*, vol. 8, no. 1, pp. 58 – 64, 1997.

[16] N. S. Poulter, W. T. E. Pitkeathly, P. J. Smith, and J. Z. Rappoport, *The Physical Basis of Total Internal Reflection Fluorescence (TIRF) Microscopy and Its Cellular Applications*, pp. 1–23. New York, NY: Springer New York, 2015.

[17] C. Smith, "Optimum single molecule localization microscopy: From single molecule detections to nanoscopic observations," 2016.

[18] B. Rieger, R. Nieuwenhuizen, and S. Stallinga, "Image processing and analysis for single-molecule localization microscopy: Computation for nanoscale imaging," *IEEE Signal Processing Magazine*, vol. 32, no. 1, pp. 49–57, 2015.

[19] A. Sharonov and R. M. Hochstrasser, "Wide-field subdiffraction imaging by accumulated binding of diffusing probes," *Proceedings of the National Academy of Sciences*, vol. 103, no. 50, pp. 18911–18916, 2006.

[20] J. Schnitzbauer, M. T. Strauss, T. Schlichthaerle, F. Schueder, and R. Jungmann, "Super-resolution microscopy with dna-paint," *Nature Protocols*, vol. 12, pp. 1198–1228, Jun 2017.

[21] P. A. Gómez-García, E. T. Garbacik, J. J. Otterstrom, M. F. Garcia-Parajo, and M. Lakadamyali, "Excitation-multiplexed multicolor superresolution imaging with fm-storm and fm-dna-paint," *Proceedings of the National Academy of Sciences*, vol. 115, no. 51, pp. 12991–12996, 2018.

[22] J. Cnossen, T. Hinsdale, R. Ø. Thorsen, M. Siemons, F. Schueder, R. Jungmann, C. S. Smith, B. Rieger, and S. Stallinga, "Localization microscopy at doubled precision with patterned illumination," *Nature Methods*, vol. 17, pp. 59–63, Jan 2020.

[23] B. Mandracchia, X. Hua, C. Guo, J. Son, T. Urner, and S. Jia, "Fast and accurate scmos noise correction for fluorescence microscopy," *Nature Communications*, vol. 11, p. 94, Jan 2020.

[24] T. Maruno, E. Toda, T. Takahashi, T. Takeshima, S. Fullerton, and K. Bennett, "Comparison of cmos and emccd cameras for computational imaging and application to superresolution localization microscopy," in *Imaging and Applied Optics Technical Papers*, p. IM4C.3, Optical Society of America, 2012.

[25] J. Joubert and D. Sharma, "Emccd vs. scmos for microscopic imaging," Mar 2011.

[26] F. Long, S. Zeng, and Z.-L. Huang, "Localization-based super-resolution microscopy with an scmos camera part ii: Experimental methodology for comparing scmos with emccd cameras," *Opt. Express*, vol. 20, pp. 17741–17759, Jul 2012.

[27] S. Cova, A. Longoni, and A. Andreoni, "Towards picosecond resolution with single-photon avalanche diodes," *Review of Scientific Instruments*, vol. 52, no. 3, pp. 408–412, 1981.

[28] F. Heide, S. Diamond, D. B. Lindell, and G. Wetzstein, "Sub-picosecond photon-efficient 3d imaging using single-photon sensors," *Scientific Reports*, vol. 8, p. 17726, Dec 2018.

[29] I. Gyongy, A. Davies, N. A. W. Dutton, R. R. Duncan, C. Rickman, R. K. Henderson, and P. A. Dalgarno, "Smart-aggregation imaging for single molecule localisation with spad cameras," *Scientific Reports*, vol. 6, p. 37349, Nov 2016.

[30] I. M. Antolovic, S. Burri, C. Bruschini, R. A. Hoebe, and E. Charbon, "Spad imagers for super resolution localization microscopy enable analysis of fast fluorophore blinking," *Scientific Reports*, vol. 7, p. 44108, Mar 2017.

[31] I. Gyongy, A. Davies, A. M. Crespo, A. Green, N. A. W. Dutton, R. R. Duncan, ..., and P. A. Dalgarno, "High-speed particle tracking in microscopy using SPAD image sensors," in *High-Speed Biomedical Imaging and Spectroscopy III: Toward Big Data Instrumentation and Management* (K. K. Tsia and K. Goda, eds.), vol. 10505, pp. 29 – 34, International Society for Optics and Photonics, SPIE, 2018.

[32] C. Bruschini, H. Homulle, and E. Charbon, "Ten years of biophotonics single-photon SPAD imager applications: retrospective and outlook," in *Multiphoton Microscopy in the Biomedical Sciences XVII* (A. Periasamy, P. T. C. So, K. König, and X. S. Xie, eds.), vol. 10069, pp. 213 – 233, International Society for Optics and Photonics, SPIE, 2017.

[33] F. Zappa, S. Tisa, A. Tosi, and S. Cova, "Principles and features of single-photon avalanche diode arrays," *Sensors and Actuators A: Physical*, vol. 140, no. 1, pp. 103 – 112, 2007.

[34] I. M. Antolovic, C. Bruschini, and E. Charbon, "Dynamic range extension for photon counting arrays," *Opt. Express*, vol. 26, pp. 22234–22248, Aug 2018.

[35] M. Fox, *Quantum optics : an introduction*. Oxford New York: Oxford University Press, 2006.

[36] S. Burri, F. Powolny, C. E. Bruschini, X. Michalet, F. Regazzoni, and E. Charbon, "A 65k pixel, 150k frames-per-second camera with global gating and micro-lenses suitable for fluorescence lifetime imaging," in *Optical Sensing and Detection III* (F. Berghmans, A. G. Mignani, and P. D. Moor, eds.), vol. 9141, pp. 55 – 61, International Society for Optics and Photonics, SPIE, 2014.

[37] I. M. Antolovic, S. Burri, C. Bruschini, R. Hoebe, and E. Charbon, "Nonuniformity analysis of a 65-kpixel cmos spad imager," *IEEE Transactions on Electron Devices*, vol. 63, pp. 57–64, Jan 2016.

[38] A. C. Ulku, C. Bruschini, I. M. Antolovic, Y. Kuo, R. Ankri, S. Weiss, X. Michalet, and E. Charbon, "A 512 × 512 SPAD image sensor with integrated gating for widefield FLIM," *IEEE Journal of Selected Topics in Quantum Electronics*, vol. 25, pp. 1–12, Jan. 2019.

[39] M. Hofbauer, B. Steindl, and H. Zimmermann, "Temperature dependence of dark count rate and after pulsing of a single-photon avalanche diode with an integrated active quenching circuit in $0.35\,\mu$m cmos," *Journal of Sensors*, vol. 2018, p. 9585931, Jul 2018.

[40] D. Neamen, *Semiconductor Physics And Devices*. McGraw-Hill, Inc., New York, USA, 2003. 3rd edition.

[41] Y. Kang, H. X. Lu, Y.-H. Lo, D. S. Bethune, and W. P. Risk, "Dark count probability and quantum efficiency of avalanche photodiodes for single-photon detection," *Applied Physics Letters*, vol. 83, no. 14, pp. 2955–2957, 2003.

[42] C. S. Smith, N. Joseph, B. Rieger, and K. A. Lidke, "Fast, single-molecule localization that achieves theoretically minimum uncertainty," *Nature Methods*, vol. 7, pp. 373–375, May 2010.

[43] A. V. Abraham, S. Ram, J. Chao, E. S. Ward, and R. J. Ober, "Quantitative study of single molecule location estimation techniques," *Opt. Express*, vol. 17, pp. 23352–23373, Dec 2009.

[44] M. Dekking, *A modern introduction to probability and statistics : understanding why and how*. London: Springer, 2005.

[45] Y. Wang, J. Schnitzbauer, Z. Hu, X. Li, Y. Cheng, Z.-L. Huang, and B. Huang, "Localization events-based sample drift correction for localization microscopy with redundant cross-correlation algorithm," *Opt. Express*, vol. 22, pp. 15982–15991, Jun 2014.

[46] F. Huang, T. M. P. Hartwich, F. E. Rivera-Molina, Y. Lin, W. C. Duim, ..., and J. Bewersdorf, "Video-rate nanoscopy using scmos camera–specific single-molecule localization algorithms," *Nature Methods*, vol. 10, pp. 653–658, Jul 2013.

[47] S. M. Kay, *Fundamentals of Statistical Signal Processing: Estimation Theory*. Upper Saddle River, NJ, USA: Prentice-Hall, Inc., 1993.

[48] A. Papoulis, *Probability, random variables, and stochastic processes*. Boston: McGraw-Hill, 2002.

Glossary

List of symbols

Symbol	Unit	Definition
c	[photons]	Photon count
F	[-]	Normalized photon count in pixel
F_n	[-]	Excess noise
g	[-]	Gain
I	[photons]	Intensity
N	[frames]	Aggregated frames
N_{RO}	[photons/s]	Readout noise
n	[px]	Number of pixels in ROI
n_i, n_1, n_2	[-]	Refractive index
t_{dead}	[s]	Deadtime
t_e	[s]	Exposure time
T_{KS}	[-]	Kolmogorov-Smirnov Statistic
V_{BD}	[V]	Breakdown voltage
V_{EX}	[V]	Excess voltage
Δl	[m]	Spatial resolution
θ_b	[photons/px]	Background noise
θ_c	[rad]	Critical incidence angle
θ_{half}	[rad]	Half angle of microscope
θ_I	[photons/m^2]	Emitter intensity
θ_x	[px]	Emitter x position
θ_y	[px]	Emitter y position
λ	[m]	Wavelength
λ_{LM}	[-]	Damping term
μ	[photons/s]	Photon rate
σ	[nm]	Standard deviation
χ^2	[-]	χ^2 statistic

List of acronyms

Acronym	Definition
APD	Avalanche photodiode
CRLB	Cramér-Rao lower bound
DCR	Dark count rate
DM	Dichroic mirror
EMCCD	Electron multiplying charge-coupled devices
FPGA	Field-programmable gated array
FWHM	Full widht at half maximum
i.i.d.	Independently and identically distributed
KS	Kolmogorov-Smirnov
meSMLM	Modulation enhanced SMLM
MLE	Maximum likelihood estimation
NA	Numerical aperture
PAINT	Point accumulation for imaging in nanoscale topography
PDE	Photon detection efficiency
PSF	Point spread function
QE	Quantum efficiency
RCC	Redundancy cross correlation
ROI	Region of interest
sCMOS	Scientific complementary metal-oxide semiconductor
SMLM	Single-molecule localization microscopy
SNR	Signal-to-noise ratio
SPAD	Single-photon avalanche diode
TIRF	Total internal reflection fluorescence